Phase Reduction Models for Improving the Accuracy of the Finite Element Solution of Time-Harmonic Scattering Problems I: General Approach and Low-Order Models

Xavier Antoine [a,b] Christophe Geuzaine [c]

[a] *Institut Elie Cartan Nancy (IECN), Nancy-Université, CNRS, INRIA Corida Team, Boulevard des Aiguillettes, B.P. 239 F-54506, Vandoeuvre-lès-Nancy Cedex, France.*

[b] *Institut National Polytechnique de Lorraine (INPL), Ecole Nationale Supérieure des Mines de Nancy, Département de Génie Industriel, Bureau 495, Parc de Saurupt, CS 14 234, 54042 Nancy Cedex, France.*

[c] *University of Liège, Department of Electrical Engineering and Computer Science, Montefiore Institute, Sart Tilman, Bldg. B28, Parking P32, B-4000, Liège, Belgium*

Abstract

This paper introduces a new formulation of high-frequency time-harmonic scattering problems in view of a numerical finite element solution. It is well-known that pollution error causes inaccuracies in the finite element solution of short-wave problems. To partially avoid this precision problem, the strategy proposed here consists in firstly numerically computing at a low cost an approximate phase of the exact solution through asymptotic propagative models. Secondly, using this approximate phase, a slowly varying unknown envelope is introduced and is computed using coarser mesh grids. The global procedure is called Phase Reduction. In this first paper, the general theoretical procedure is developed and low-order propagative models are numerically investigated in detail. Improved solutions based on higher order models are discussed showing the potential of the method for further developments.

Key words: Helmholtz equation, acoustic scattering, short-wave problem, finite element method, pollution, accuracy, On-Surface Radiation Condition method
PACS:

1 Introduction

The purpose of this paper is to investigate simple evolution models for exterior scattering problems around convex obstacles, and use these models to reduce the pollution error in the finite element solution of time-harmonic scattering problems.

The pollution error finds its origin in the oscillatory nature of the solution of such scattering problems, and is deeply linked to the loss of stability of the Helmholtz operator for high wavenumbers. As evidenced by Babuska *et al.* [31,22,23], the contribution of the pollution error to the overall error in the finite element solution of scattering problems thus becomes predominant at high wavenumbers k. This requires to increase the mesh density faster than the wavenumber to maintain a prescribed accuracy [33], and leads to intractable computational costs at very high frequencies, i.e., when the wavelength $\lambda = 2\pi/k$ is much smaller than the characteristic length of the geometrical structure.

Several techniques have been proposed during the last decade to overcome this problem: *hp* finite element methods, stabilized Galerkin finite element methods, multi-scales techniques, wave-based discretization techniques, etc. We cannot mention here the numerous papers related to all these improvements and instead refer the reader to the recent review by Thompson [33] for further details and references.

A common point between all these techniques lies in the fact that information about the scattering problem is incorporated into the finite element procedure. One popular approach is to replace the standard polynomial basis functions by plane wave functions [26,19]. Another viewpoint [9–12,7,8,15,17,34], which we adopt in this paper, is to approximate the phase of the solution and use this phase to reformulate the problem in terms of a slowly oscillatory envelope. If we denote the solution of the original scattering problem by u, this approach thus involves a two-fold solution process:

1) find an approximation $\widetilde{\phi}$ of the phase ϕ of u in the whole computational domain;
2) use $\widetilde{\phi}$ to solve the scattering problem in terms of a new, slowly varying unknown.

This has the advantage that the resulting formulation can be easily coded into a classical finite element solver and does not require any integration of new basis functions. Moreover, this technique is not restricted to the finite element method, and can be used in other numerical schemes like finite difference, integral or spectral methods.

In this paper, we propose an original approach for solving point 1) above, i.e., to find an approximation of the phase of the highly-oscillatory solution in the computational domain. Our approach is based on three main ingredients:

1.a) first, we build an initial condition on the surface of the scatterer (that we call the *starter*);
1.b) then, we construct an approximate pseudo-differential evolution operator (that we call the *propagator*) to extend the starter into the exterior computational domain;
1.c) and finally, to reduce the computational cost, we localize the propagator using purely differential operators.

We then solve an alternative variational problem, equivalent to the original one, by using the phase $\widetilde{\phi}$ of the approximate solution. The new unknown is expected to oscillate less than the original one, which permits to significantly reduce the pollution error, or, alternatively, to obtain the same accuracy as the classical finite element method with coarser discretizations. We call the resulting technique the *Phase Reduction* procedure (or PR for short). It can be seen as a numerical extension of asymptotic approaches like the WKB approximation [13], with the added advantage that, provided that the finite element mesh resolves the amplitude, the method results in a convergent solution of the original problem—even if the phase approximation is inaccurate. To some extend, the PR procedure can also be seen as a general extension of the concept of Wave Envelope introduced by Baumeister [9–12] for treating particular guided waves propagation problems, and later used by Astley and Everman [7,8] for acoustical radiation.

To show the potential our approach, in this paper we mainly consider the *lowest order* (and computationally simplest) models associated with points 1.a), 1.b) and 1.c) above. Even with these low order approximations, we will show that significant improvements can be achieved on general scattering problems around convex obstacles. Improvements that can be expected at very high frequencies using higher order models are also briefly presented.

The paper is structured as follows: in Section 2 we outline our phase reduction strategy on a simple one-dimensional scattering problem. In Section 3 we present the usual variational formulation for higher-dimensional scattering problems, using a Bayliss-Gunzburger-Turkel-like radiation condition to truncate the infinite domain. The phase reduction procedure for higher-dimensional scattering problems is then detailed in Section 4, and Section 5 provides numerical simulations to show the improvements related to the phase reduction approach. In Section 6 we show the improvements that can be expected at very high frequencies by using higher order models.

2 The one-dimensional case: a simple and explicit example

Assume that we wish to solve the one-dimensional Neumann scattering problem

$$\begin{aligned} \partial_x^2 u + k^2 u &= 0, \qquad \text{in } \Omega_b =]0,1[, \\ \partial_{\boldsymbol{n}_\Gamma} u &= ik, \qquad \text{at } \Gamma = \{0\}, \\ \partial_x u - iku &= 0, \qquad \text{at } \Sigma = \{1\}. \end{aligned} \tag{1}$$

The above boundary-value problem corresponds to the solution of the scattering of a one-dimensional incident plane wave by the left half-space, introducing an exact transparent boundary condition on the fictitious boundary $\Sigma = \{1\}$. This non-reflecting boundary condition is given through the Dirichlet-to-Neumann (DtN) operator $\Lambda = ik$ on Σ by the relation: $\partial_x u = \Lambda u$.

2.1 The pollution problem

It is well-known since the pioneering works of Babuska and Ihlenburg [22,23,33,21] that the finite element approximation of the solution $u(x) = e^{ikx}$ of problem (1) suffers from numerical pollution, especially for large wavenumbers k. Essentially, this is related to the inadequacy of the polynomial finite element basis used to represent the unknown wavefield. To clarify this problem, we consider the covering of the computational bounded domain Ω_b using N_h uniform segments of length h, setting $h = 1/N_h$. We report in Figure 1 the exact solution u and its linear finite element approximation u_h for $k = 40$. We denote by $n_\lambda = \lambda/h$ the density of discretization points per wavelength λ. As we can see in Figure 1, a density $n_\lambda = 8$ is too small to compute an accurate approximate solution. The usual rule of thumb of "10 points per wavelength" is generally not sufficient and a mesh refinement is required, resulting in an added computational cost. This loss of accuracy is known as pollution and translates the accumulation of numerical phase error over the computational domain inherent in the FEM. Classical error estimates can be derived (see e.g. [33,21]) to quantify this pollution error, which becomes predominant compared to the approximation error for large wavenumbers.

2.2 A possible strategy to reduce the pollution error

To partially avoid the pollution error, we investigate in this paper the procedure based on the two following successive steps:

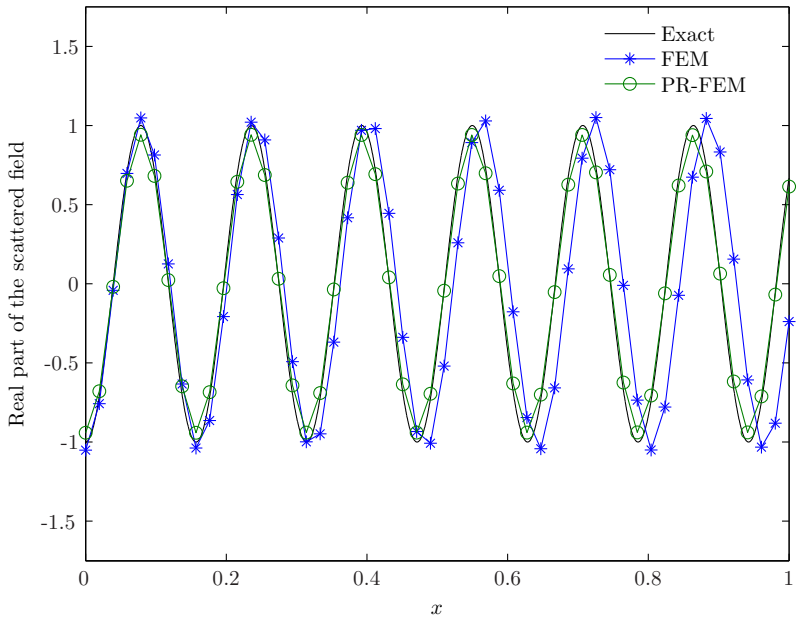

Fig. 1. Real part of the scattered field at a frequency $k = 40$ for a density of discretization points $n_\lambda = 8$. The pollution effect can be observed on the classical FEM approach but is avoided by the PR-FEM formulation.

1) The first step consists in determining an approximate solution

$$\widetilde{u} = \widetilde{A}(x)e^{ik\widetilde{\phi}(x)} \tag{2}$$

in the whole computational domain Ω_b as the solution of an evolution equation (the propagator) in the x-direction, with an initial condition to be determined on Γ (the starter); once the approximate field (2) is known in the volumetric computational domain, we extract its phase $\widetilde{\phi}(x)$.

2) The second step consists in solving a new variational formulation for the approximate slowly varying complex-valued envelope $\mathbb{A}(x)$ of the true solution $u(x) = \mathbb{A}(x)e^{ik\widetilde{\phi}(x)}$, setting

$$\mathbb{A}(x) = A(x)e^{ik(\phi(x)-\widetilde{\phi}(x))}, \tag{3}$$

where A and ϕ respectively designate the true real-valued amplitude and phase of u:

$$u(x) = A(x)e^{ik\phi(x)}. \tag{4}$$

Following this strategy, the pollution error is expected to be reduced since an approximate *a priori* phase determination leads to the computation of a slowly varying field $\mathbb{A}$.

2.2.1 Computing the approximate solution $\widetilde{u}$

The solution of step 1) is split in two distinct problems:

1.a) the construction of the starter;
1.b) the obtention of the propagator.

Point 1.a) is solved through the following considerations. From the nature of the scattering problem (1), the Neumann boundary condition is given. To get an approximate starting field, we apply the transparent boundary condition directly at the physical boundary Γ. In other words, we consider the so-called *On-Surface Radiation Condition* (OSRC) [3,25] solution in the one-dimensional case. In our simple situation, this condition is *exact* and gives the initial wavefield $\widetilde{u}_0$ as

$$\widetilde{u}_0 = \widetilde{u}(0) = (ik)^{-1}\partial_{\boldsymbol{n}_\Gamma} u = 1, \qquad \text{at } \Gamma. \tag{5}$$

Interpreting x as a time variable, the equation (5) is an initial condition.

In the case of a Dirichlet boundary condition $u = f$ on Γ, the initial condition is directly given by $\widetilde{u}_0 = f$ on Γ and hence does not require the help of the OSRC technique [17].

Let us now consider point 1.b). To construct the propagator, we rewrite the Helmholtz equation under its (exact) factorized form

$$(\partial_x^2 + k^2)u = (\partial_x + i\mathcal{P}^-)(\partial_x + i\mathcal{P}^+)u = 0, \qquad \text{for } x \geq 0, \tag{6}$$

setting $\mathcal{P}^\pm = \mp k$. The solution of the evolution equation

$$\partial_x \widetilde{u} + i\mathcal{P}^+ \widetilde{u} = 0 \tag{7}$$

corresponds to the forward propagative wave and is considered as our propagator. The solution $\widetilde{u}$ of (7) with the initial condition (5) can be directly obtained as $\widetilde{u} = e^{ikx}\widetilde{u}_0 = e^{ikx}$.

The procedure consisting in writing an approximate forward propagating model is closely related to the techniques employed in optics, underwater or electromagnetic wave propagation and better known under the denominations respectively of Beam Propagation Methods (BPM) [28] or parabolic equations [27]. As discussed next, the situation is more complicated in higher dimensions since the wavefield propagates from a (usually) *curved* surface Γ.

2.2.2 Computing the true solution u

The second step of the algorithm consists in solving an equation for $\mathbb{A}$ defined by:

$$\mathbb{A} = e^{-ik\widetilde{\phi}} u. \tag{8}$$

Again, in the considered configuration, we know that $u(x) = e^{ikx}$ and consequently that $\mathbb{A}(x) = 1$ since $\widetilde{\phi}(x) = x$. Therefore, $\mathbb{A}$ is a slowly varying

envelope and the polynomial basis functions lead to an optimal numerical computation. However, to explain in detail the real strategy considered for higher dimensions, we rather proceed as follows. The variational formulation of problem (1) is given by: find $u \in H^1(\Omega_b)$ such that

$$\int_{\Omega_b} \left\{ \partial_x u \, \partial_x \bar{v} - k^2 u \bar{v} \right\} dx - ik(u\bar{v})(1) = -(g\bar{v})(0), \qquad \forall v \in H^1(\Omega_b). \tag{9}$$

Since $\mathbb{A}$ is defined by (8), with $\widetilde{\phi}$ known from step 1), we replace u in the weak formulation (9) using $u = e^{ik\widetilde{\phi}}\mathbb{A}$, and we choose some test-functions v defined by $v = e^{ik\widetilde{\phi}}\mathbb{B}$. Using these relations, we get the new formulation: find $\mathbb{A} \in H^1(\Omega_b)$ such that

$$\int_{\Omega_b} \left\{ \partial_x \mathbb{A} \, \partial_x \bar{\mathbb{B}} + ik\partial_x\widetilde{\phi}(\mathbb{A}\partial_x\bar{\mathbb{B}} - \bar{\mathbb{B}}\partial_x\mathbb{A}) - k^2(1 - |\partial_x\widetilde{\phi}|^2)\mathbb{A}\bar{\mathbb{B}} \right\} dx \\ - ik(\mathbb{A}\bar{\mathbb{B}})(1) = -(f\bar{\mathbb{B}})(0), \qquad \forall \mathbb{B} \in H^1(\Omega_b), \tag{10}$$

where $f(0) = e^{-ik\widetilde{\phi}(x)_{|x=0}} g(0) = ik$. This formulation is nothing else than the weak formulation of the initial boundary-value problem (1) with $\mathbb{A}$ as the new unknown. The weak formulation (10) is easy to implement in a finite element code and only requires some elementary modifications of the initial formulation (9). The FEM solution to formulation (10) will be referred to as *Phase-Reduction FEM* (PR-FEM) in the sequel. We present in Figure 1 the computed discrete finite element solution based on $\mathbb{A}$ using (10). We observe that we avoid any pollution fundamentally because we compute a non oscillatory solution. The polynomial representation is therefore optimal.

The goal of the following sections is to extend this approach to scattering problems in higher dimensions, where the computation of $\widetilde{u}$ can only be realized in an *approximate* way. In this case, we cannot completely avoid the pollution error in the finite element solution, but we can expect to *reduce* it significantly at high wavenumbers. Furthermore, the extension to variable wavenumbers can also be considered. Indeed, the construction based on pseudodifferential operators and presented in the next section enable one to consider Helmholtz equations with variable coefficients.

3 The classical variational formulation for higher dimensions

We investigate the numerical solution of the time-harmonic acoustic scattering problem of a plane wave $u^{\rm inc}(\boldsymbol{x}) = e^{ik\boldsymbol{\alpha}\cdot\boldsymbol{x}}$, $|\boldsymbol{\alpha}| = 1$, by a sound-hard or a sound-soft convex obstacle $\Omega^- \subset \mathbb{R}^d$, $d > 1$, with a $\mathcal{C}^1$ closed boundary Γ. We set $\Omega^+ := \mathbb{R}^d \backslash \overline{\Omega^-}$ as the exterior domain of propagation associated with Ω^-. The spatial variable is denoted by $\boldsymbol{x} = (x_1, ..., x_d)$. The boundary value problem

reads:

$$\begin{aligned} \Delta u + k^2 u = 0, \qquad & \text{in } \Omega^+, \\ \partial_{\boldsymbol{n}_\Gamma} u = g := -\partial_{\boldsymbol{n}_\Gamma} u^{\text{inc}} \quad \text{or} \quad u = f := -u^{\text{inc}}, \qquad & \text{on } \Gamma, \\ \lim_{|\boldsymbol{x}|\to+\infty} |\boldsymbol{x}|^{(d-1)} (\nabla u \cdot \frac{\boldsymbol{x}}{|\boldsymbol{x}|} - iku) = 0. & \end{aligned} \tag{11}$$

The operator Δ is the Laplacian operator and $\boldsymbol{a} \cdot \boldsymbol{b}$ designates the hermitian inner product of two d-dimensional complex-valued vector fields $\boldsymbol{a}$ and $\boldsymbol{b}$. The outwardly directed unit normal vector to Ω^- is $\boldsymbol{n}_\Gamma$. In a suitable functional setting, this problem is known to be well-posed [16].

Let us begin by introducing the classical weak formulation and the finite element method to solve (11). We consider a smooth convex fictitious boundary Σ enclosing the scatterer Ω^- and we set Ω_b as the bounded computational domain delimited by Γ and Σ. Since our aim here is not to investigate all the available solutions to bound the computational domain, we only consider the second-order Bayliss-Gunzburger-Turkel-like (BGT2-like) Artificial Boundary Condition (ABC) derived in [4]. Other truncation techniques like PML [14,20] could also be used and adapted as easily to the proposed strategy. The BGT2-like ABC on Σ is given by

$$\partial_{\boldsymbol{n}_\Sigma} u = \mathcal{B} u, \qquad \text{on } \Sigma, \tag{12}$$

where $\mathcal{B}$ is a second-order symmetrical tangential boundary operator and $\boldsymbol{n}_\Sigma$ designates the outwardly directed unit normal vector to Σ. To simplify the notations, we keep on denoting by u the solution of the approximate model with the BGT2-like ABC (see system (16)) even if this function is obviously different from the solution of the initial problem (11). The boundary operator $\mathcal{B}$ is given by

$$\mathcal{B} u = \text{div}_\Sigma (A \nabla_\Sigma u) - \beta u, \qquad \text{on } \Sigma, \tag{13}$$

where the operator div_Σ is the surface divergence of a tangential complex-valued vector field and ∇_Σ is the surface gradient operator of a complex-valued scalar surface field, all these quantities being defined over Σ. Furthermore, the operator A is the complex-valued tensor field given by

$$A = -\frac{1}{2ik} (\mathbb{I} + \frac{i\mathcal{R}}{k})^{-1} \tag{14}$$

and β is the complex-valued scalar function

$$-ik + \mathcal{H} + \frac{i}{2k} (1 + \frac{2\mathcal{H}}{k})^{-1} (\mathcal{K} - \mathcal{H}^2) - \frac{\Delta_\Gamma \mathcal{H}}{4k^2}. \tag{15}$$

In the above notations, the operator $\mathbb{I}$ is the identity operator of the tangent plane and $\mathcal{R}$ is the curvature tensor. We denote by $\mathcal{H}$ and $\mathcal{K}$ respectively the mean and Gauss curvatures. The Laplace-Beltrami operator is $\Delta_\Sigma u =$

$\mathrm{div}_\Sigma(\nabla_\Sigma u)$. It results that the truncated boundary-value problem is given by

$$\begin{aligned} \Delta u + k^2 u = 0, &\qquad \text{in } \Omega_b, \\ \partial_{\boldsymbol{n}_\Gamma} u = g \quad \text{or} \quad u = f, &\qquad \text{on } \Gamma, \\ \partial_{\boldsymbol{n}_\Sigma} u = \mathcal{B} u, &\qquad \text{on } \Sigma. \end{aligned} \tag{16}$$

For the Neumann problem, the variational formulation consists in computing $u \in H^1(\Omega_b)$ such that

$$a(u, v) = \ell(v), \tag{17}$$

for any test-function $v \in H^1(\Omega_b)$. The sesquilinear form $a(\cdot, \cdot)$ is defined by

$$a(u, v) = (\nabla u, \nabla v)_{0,\Omega_b} - k^2 (u, v)_{0,\Omega_b} + (A \nabla_\Sigma u, \nabla_\Sigma v)_{0,\Sigma} + (\beta u, v)_{0,\Sigma} \tag{18}$$

and the linear form ℓ appearing in the right-hand side is

$$\ell(v) = -(g, v)_{0,\Gamma}. \tag{19}$$

We define $(\cdot, \cdot)_{0,D}$ as the hermitian inner product of two complex-valued square-integrable functions u and v of $L^2(D)$

$$(u, v)_{0,D} = \int_D u \bar{v} dD, \tag{20}$$

where D specifies the integration domain. In the case of two complex-valued vector fields $\boldsymbol{u}$ and $\boldsymbol{v}$ defined on D, the inner product is

$$(\boldsymbol{u}, \boldsymbol{v})_{0,D} = \int_D \boldsymbol{u} \cdot \bar{\boldsymbol{v}} dD. \tag{21}$$

The finite element solution consists in introducing a covering Ω_h of Ω_b using some tetrahedrons K: $\Omega_h = \cup_{K \in \mathcal{K}_h} K$, where $\mathcal{K}_h$ designates a triangulation of the domain. The corresponding interpolated boundaries associated with Γ and Σ are respectively denoted by Γ_h and Σ_h. The p-finite element version of (17) yields the discrete formulation: find $u_h \in V_h$ such that

$$a_h(u_h, v_h) = \ell_h(v_h), \tag{22}$$

for any test-function v_h of V_h, setting

$$\begin{aligned} a_h(u_h, v_h) = (\nabla u_h, \nabla v_h)_{0,\Omega_h} - k^2 (u_h, v_h)_{0,\Omega_h} \\ + (A_h \nabla_{\Sigma_h} u_h, \nabla_{\Sigma_h} v_h)_{0,\Sigma_h} + (\beta_h u_h, v_h)_{0,\Sigma_h} \end{aligned} \tag{23}$$

and

$$\ell_h(v_h) = -(g_h, v_h)_{0,\Gamma_h}. \tag{24}$$

The classical finite element space of order p is given by

$$V_h := \{ v_h \in \mathcal{C}^0(\overline{\Omega_h}) / v_{h\ |K} \in \mathbb{P}_p(K), \forall K \in \mathcal{K}_h \}, \tag{25}$$

where $\mathbb{P}_p$ denotes the space of polynomials of degree less than or equal to p. The approximate fields A_h and β_h are computed by some suitable schemes based on the surface mesh. We refer to [1] for implementation details. Finally, the solution of (22) leads to the solution of a linear system

$$[a_h]\boldsymbol{u}_h = \boldsymbol{b}_h, \tag{26}$$

where $[a_h]$ is a non-hermitian complex-valued matrix of size $N_h \times N_h$, $\boldsymbol{u}_h$ and $\boldsymbol{b}_h$ are two complex-valued vectors of $\mathbb{C}^{N_h}$, and N_h is the number of degrees of freedom associated with the finite element approximation. The whole procedure is referred to as FEM in what follows.

Concerning the Dirichlet problem, a similar weak formulation can be obtained in a classical way. We do not detail here this point which is immediate.

4 The Phase Reduction formulation for higher dimensions

We now detail our strategy to solve the two successive steps outlined in the introduction for higher dimensions. Point 1) is developed in Section 4.1 (more specifically, Section 4.1.1 deals with the proposition of a starter, i.e., Point 1.a), while Section 4.1.2 concerns the construction of the propagator, i.e., Point 1.b)). For now we only consider the lowest order propagator and therefore Point 1.c) is direct—improvements will be considered later in Section 6. Point 2) is developed in Section 4.2.

We focus the presentation on the sound-hard case, i.e., on the problem with a Neumann boundary condition. Like in the one-dimensional case, the PR-FEM for the Dirichlet problem is obtained in a similar way, with the added simplification that the starter is obtained immediately from the boundary condition. Preliminary results for the two-dimensional Dirichlet scattering problem were presented in the short paper [17].

4.1 Computing the approximate solution $\widetilde{u}$

4.1.1 Construction of the initial condition $\widetilde{u}_0$ (starter)

In the one-dimensional case, we have seen that the construction of the initial condition is essentially based on the knowledge of the Dirichlet-to-Neumann (DtN) operator Λ on Γ. This approach, called the On-Surface Radiation Condition method, has been formally introduced in the middle of the eighties by Kriegsmann, Taflove and Umashankar [25] for the computation of an electromagnetic wave by a perfectly conducting body. Since then, numerous im-

provements and generalizations have been developed both in acoustics and electromagnetism. We restrict our presentation here to the use of the OSRC method applied to the construction of the initial condition at high frequencies. We refer to [3] for a recent presentation of the OSRC approach and its applications. An interesting aspect of the OSRC approach is that the construction of the approximate solution is not based on only taking into account the Helmholtz operator but rather on considering the complete scattering boundary value problem. In this sense, the OSRC method provides an approximate solution which has a behavior close to the true solution and can be seen as a numerical asymptotic solution for a general scattering problem.

The accuracy and efficiency of these techniques are deeply related to the way of constructing the approximation of the DtN map. Various choices exist and are in some way all related to a subjacent (local or microlocal) asymptotic analysis. Since we wish to solve a high frequency scattering problem, we choose the square-root OSRC proposed in [5]. For a given normal derivative trace on Γ, this operator expresses an approximation φ of the exact trace of the solution u through the relation

$$\partial_{\boldsymbol{n}_\Gamma} u = \Lambda\varphi, \qquad \text{on } \Gamma, \tag{27}$$

where Λ is the pseudo-local OSRC operator given by

$$\Lambda = ik\sqrt{1+X}. \tag{28}$$

In our case, we will set $\widetilde{u}_0 = \varphi$. The symmetrical partial differential operator X is

$$X = \mathrm{div}_\Gamma(k_\varepsilon^{-2}\nabla_\Gamma\cdot), \tag{29}$$

defining the complex wavenumber k_ε as $k_\varepsilon = k + i\varepsilon$, with $\varepsilon = 0.4k^{1/3}\mathcal{H}_\Gamma^{2/3}$, where $\mathcal{H}_\Gamma$ is the mean curvature on Γ. Since the operator is non-local like in the integral equation approach, its numerical inversion is computationally expensive. However, its simulation can be efficiently carried out by using a suitable complex Padé approximant of the square-root $\sqrt{z}$ of a complex number z. The principal determination of the square-root is considered with a branch-cut along the negative real axis. Following [5], we use the approximation described in [29]

$$\sqrt{1+z} \approx e^{i\theta/2} R_{N_p}(e^{-i\theta}(1+z)-1) = A_0 + \sum_{j=1}^{N_p} \frac{A_j z}{1+B_j z}, \tag{30}$$

setting

$$A_j = \frac{e^{-i\theta/2} a_j}{(1+b_j(e^{-i\theta}-1))^2} \qquad \text{and} \qquad B_j = \frac{e^{-i\theta} b_j}{1+b_j(e^{-i\theta}-1)}, \tag{31}$$

and $A_0 = e^{i\theta/2} R_{N_p}(e^{-i\theta}-1)$. The function R_{N_p} designates the usual real Padé

approximant of order N_p of the square-root defined by

$$\sqrt{1+z} \approx R_{N_p}(z) = 1 + \sum_{j=1}^{N_p} \frac{a_j z}{1 + b_j z}, \tag{32}$$

with the coefficients

$$a_j = \frac{2}{2N_p+1} \sin^2(\frac{j\pi}{2N_p+1}) \qquad \text{and} \qquad b_j = \cos^2(\frac{j\pi}{2N_p+1}). \tag{33}$$

In the sequel, we take the optimal values $N_p = 8$ and $\theta = \pi/3$ considered in [5]. The important feature in using a Padé interpolant is that the approximate and accurate application of the operator (28) to a given surface function ψ can be realized through the solution of $(N_p + 1)$ complex-valued coefficients Helmholtz-type partial differential equations over Γ. Indeed, we can reformulate the problem of evaluating $\Psi = \Lambda\psi$ as the application of the Padé-type operator to a given datum ψ applying the following procedure: solve the N_p surface partial differential equations with respect to the auxiliary unknowns ψ_j through the variational formulation

$$\int_\Gamma \frac{B_j}{k_\varepsilon^2} \nabla_\Gamma \psi_j \cdot \nabla_\Gamma \varphi - \psi_j \varphi d\Gamma + \int_\Gamma \psi \varphi d\Gamma = 0, \qquad 1 \leq j \leq N_p, \tag{34}$$

and next compute Ψ variationally using

$$\int_\Gamma \Psi \varphi d\Gamma = ikA_0 \int_\Gamma \psi \varphi d\Gamma - ik \sum_{j=1}^{N_p} \int_\Gamma \frac{A_j}{k_\varepsilon^2} \nabla_\Gamma \psi_j \cdot \nabla_\Gamma \varphi d\Gamma. \tag{35}$$

In the above relations, φ designates a suitable test-function defined on Γ. In our case, we adapt easily this procedure to Equation (27) by rewriting the pseudodifferential equation as

$$\int_\Gamma \Lambda g \varphi d\Gamma = \int_\Gamma \frac{k^2}{k_\varepsilon^2} \nabla_\Gamma \widetilde{u}_0 \cdot \nabla_\Gamma \varphi - k^2 \widetilde{u}_0 \varphi d\Gamma. \tag{36}$$

This formulation only requires the solution to an additional surface partial differential equation over Γ. All these equations can be solved efficiently [5] by using a discretization based on a surface finite element method on Γ_h. Let us introduce N_{Γ_h} as the number of degrees of freedom arising in the surface finite element method. Then, the resulting linear systems defining the OSRC through the Padé approximants can be solved at a linear cost according to N_{Γ_h} by a preconditioned ILUT Krylov iterative solver [30]. All this process yields the efficient construction of the approximate initial condition $\widetilde{u}_0$ on the boundary Γ. The theory of OSRCs assumes that Ω^- is a convex domain [3]. Some coupling procedures exist to extend its application range to non-convex bodies [2], which we won't consider here. Finally, an explicit analytical starter

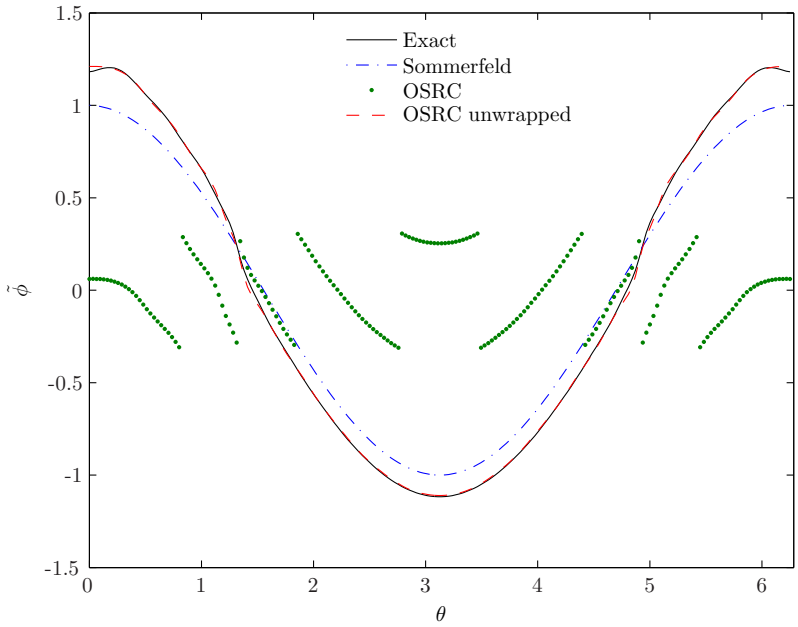

Fig. 2. Surface phase $\widetilde{\phi}$ for the Neumann problem and the unit circular cylinder at $k = 10$: exact solution, Sommerfeld solution, high-order OSRC and unwrapped high-order OSRC solutions.

$\widetilde{u}$ is obtained if one uses the lowest-order approximation called Sommerfeld approximation

$$\widetilde{u} = -i\partial_{\boldsymbol{n}_\Gamma} u/k, \qquad \text{on } \Gamma. \tag{37}$$

This approximation will be used in the numerical tests presented in Section 5. We will see that it yields interesting but also limited accuracy improvements for high wavenumbers and/or coarse meshes. Section 6 will reveal the interest of numerically using high-order models like the Padé model introduced above if high-order propagators are considered at the same time.

Once the surface field $\widetilde{u}_0$ is known on Γ, the corresponding surface phase function $\widetilde{\phi}$ can be computed. This is of interest in the sequel since we use a low-order propagation model giving an explicit phase function $\widetilde{\phi}$ over the computational domain once its trace is known (through Equation (50)). If one uses the solution which consists in writing the phase at a surface point using the relation

$$\widetilde{\phi} = \frac{1}{ik} \log(\frac{\widetilde{u}_0}{\widetilde{A}}), \qquad \text{for } \widetilde{u}_0 \neq 0, \tag{38}$$

the resulting calculation yields a discontinuous determination of the phase since the exponential function is a periodic function. A test example of such a problem is given on Figure 2 in the simple case of a circular cylinder at $k = 10$ for the Neumann boundary condition. This difficulty is known as the phase unwrapping problem. This is an important point to deal with in our approach because the involvement of a discontinuous phase in the weak variational formulation on $\mathbb{A}$ (see for example Equations (51)-(52)) would clearly lead to difficulties in the finite element solution. To solve this problem, we use the

following strategy. Consider the known field $\widetilde{u}_0$ and differentiate the relation $e^{ik\widetilde{\phi}} = \widetilde{u}_0/\widetilde{A}$ assuming that the surface field is not equal to zero. Taking the real part of the equation, one gets

$$\nabla_\Gamma \widetilde{\phi} = \boldsymbol{F} := \Re\left(\frac{1}{ik}\frac{\widetilde{A}}{\widetilde{u}_0}\nabla_\Gamma\left(\frac{\widetilde{u}_0}{\widetilde{A}}\right)\right), \tag{39}$$

where the surface vector field $\boldsymbol{F}$ is known. If one fixes the value of $\widetilde{\phi}$ at an arbitrary surface point $\boldsymbol{x}^*$ where $\widetilde{u}_0$ is non-zero and one takes the surface divergence of the equation (39), then, a continuous determination of the phase $\widetilde{\phi}$ can be computed as the unique solution to the well-posed surface partial differential equation

$$\begin{cases} -\Delta_\Gamma \widetilde{\phi} = -\mathrm{div}_\Gamma \boldsymbol{F}, & \text{on } \Gamma, \\ \widetilde{\phi}(\boldsymbol{x}^*) = \arg\left(\dfrac{\widetilde{u}_0(\boldsymbol{x}^*)}{\widetilde{A}(\boldsymbol{x}^*)}\right). \end{cases} \tag{40}$$

The numerical solution can be easily obtained by a surface finite element method, similarly to the OSRC technique, by the formulation

$$\int_\Gamma \nabla_\Gamma \widetilde{\phi} \cdot \nabla_\Gamma \varphi d\Gamma = -\int_\Gamma \mathrm{div}_\Gamma(\boldsymbol{F})\varphi d\Gamma, \tag{41}$$

for some test-functions φ and fixing the value of $\widetilde{\phi}$ at a surface point $\boldsymbol{x}^*$. This process yields a continuous phase $\widetilde{\phi}$ over the surface Γ, as shown on Figure 2 where we see the unwrapped version of the phase for our previous example, computed using the high-order OSRC solution. We also see the accuracy improvement related to the choice of the OSRC.

4.1.2 Construction of the evolution equation (propagator): general approach and low-order approximation

The next step of the approach consists in developing an approximate forward propagating equation called the propagator. Unlike the one-dimensional case, the situation is much more complex because of the boundary. We propose here a general construction of an approximate DtN map using pseudodifferential operators theory and elements developed in [4]. We will use its lowest order approximation for the PR-FEM computations performed in Section 5 but will show in Section 6 that it is crucial to consider the proposed high-order models to investigate improved solutions at high-frequency and for coarse meshes.

Let us consider a point $\boldsymbol{x}$ in Ω_b (or more generally in Ω^+). Since Ω^- is convex, any observation point $\boldsymbol{x}$ can be projected onto Γ as a unique point $\boldsymbol{x}_0 = \pi_\Gamma \boldsymbol{x} \in \Gamma$, where π_Γ is the projection operator onto Γ. Let us introduce $\boldsymbol{r} = \boldsymbol{x}_0\boldsymbol{x}$ and $r = \|\boldsymbol{r}\|$. The outwardly directed unit normal vector to Γ

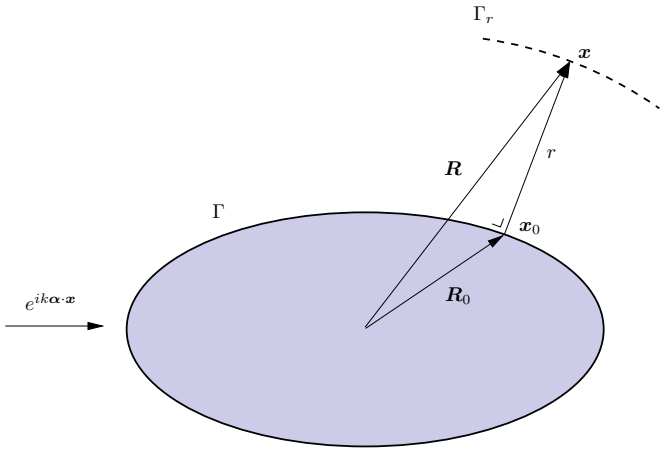

Fig. 3. Illustration of the notations used in the construction of the forward propagating model.

at point $\boldsymbol{x}_0$ is given by $\boldsymbol{n}_\Gamma(\boldsymbol{x}_0) = \boldsymbol{r}/r$ (see Fig. 3). Since Γ is a compact submanifold of $\mathbb{R}^d$, a local coordinates system at a point $\boldsymbol{x}_0$ of Γ can be chosen. Let us introduce the tangential variable $\boldsymbol{s} = (s_1, s_2)$ and the radial variable r along $\boldsymbol{n}_\Gamma(\boldsymbol{x}_0)$, setting $r = 0$ at $\Gamma = \Gamma_0$ and Γ_r for the parallel surface. We choose an orthogonal coordinates system on Γ. The covariant basis $(\boldsymbol{\tau}_1, \boldsymbol{\tau}_2)$ of the tangent plane $T_{\boldsymbol{x}_0}(\Gamma)$ compatible with the orientation of $\boldsymbol{n}(\boldsymbol{x}_0)$ is better known as the principal basis, where $\boldsymbol{\tau}_1$ and $\boldsymbol{\tau}_2$ are the principal directions of curvatures to the surface. Setting $\mathcal{R}_\Gamma$ as the curvature tensor of the tangent plane at a given point of the surface, the principal curvatures κ_1 and κ_2 of Γ satisfy: $\mathcal{R}_\Gamma \tau_\beta = \kappa_\beta \tau_\beta$, for $\beta = 1, 2$, and the mean curvature $\mathcal{H}_\Gamma = trace(\mathcal{R}_\Gamma)/2$. Introducing the functions $h_\beta = 1 + r\kappa_\beta$, $\beta = 1, 2$, we get the expression of the Helmholtz operator in generalized coordinates

$$L(r, s, \partial_r, \partial_s)u = \partial_r^2 + 2\mathcal{H}_r \partial_r + h_1^{-1} h_2^{-1} \partial_s \cdot (h_2 h_1^{-1} \partial_{s_1}, h_1 h_2^{-1} \partial_{s_2}) + k^2, \quad (42)$$

setting $\mathcal{H}_r = (h_1^{-2}\kappa_1 + h_2^{-2}\kappa_2)$. Now adapting the techniques used in [4], we prove the existence and uniqueness of two pseudodifferential operators $\mathcal{P}^\pm$ such that the equation

$$(\partial_r + i\mathcal{P}^+)\widetilde{u} = 0, \qquad \text{on } \Gamma_r, \quad (43)$$

characterizes the forward propagating part of the wavefield. The other operator $\mathcal{P}^-$ yields the reentrant part of the field to Γ_r. Let us introduce the total symbols $p^\pm(r, \boldsymbol{s}, \boldsymbol{\xi}) = \sigma_{\mathcal{P}^\pm}$ of $\mathcal{P}^\pm = \mathcal{P}^\pm(r, \boldsymbol{s}, \partial_{\boldsymbol{s}})$, setting $\boldsymbol{\xi} = (\xi_1, \xi_2)$ as the Fourier covariable of $\boldsymbol{s}$. These two symbols admit a unique asymptotic expansion in homogeneous symbols $\left\{p_{-j}^\pm\right\}_{j \geq -1}$ of order $-j$ as

$$p^\pm \sim \sum_{j \geq -1} p_{-j}^\pm, \quad (44)$$

where the functions $p_{-j}^\pm$ satisfy: $p_{-j}^\pm(r, \boldsymbol{s}, \lambda\boldsymbol{\xi}) = \lambda^{-j} p_{-j}^\pm(r, \boldsymbol{s}, \boldsymbol{\xi})$, $\forall \lambda > 0$ (see [32] for the definition of $\sim$). The uniqueness of the expansion is fixed through

the condition on the principal symbol

$$p_1^{\pm} = \mp\sqrt{k^2 - ||\boldsymbol{\xi}||^2}, \tag{45}$$

setting $||\boldsymbol{\xi}||^2 = h_1^{-2}\xi_1^2 + h_2^{-2}\xi_2^2$. Now if one considers for example the approximation of (43) by the equation

$$(\partial_r + i\mathrm{Op}(p_1^+))\widetilde{u} = 0, \qquad \text{on } \Gamma_r, \tag{46}$$

we obtain a nonlocal propagation equation to solve ($\mathrm{Op}(\sigma)$ designates the pseudodifferential operator with symbol σ). Using the symbol (45) leads to a correct computation of propagative modes but can exhibit a loss of accuracy for high-order spatial frequencies $\boldsymbol{\xi}$ such that $||\boldsymbol{\xi}|| \approx k$ since it is singular. A regularization (like in the OSRC technique) of p_1^+ must be considered. In the same spirit as in [5], we take:

$$p_{1,\eta}^+ = -k\sqrt{1 - \frac{||\boldsymbol{\xi}||^2}{k_\eta^2}}, \tag{47}$$

setting $k_\eta = k + i\eta$, with $\eta = 0.4k^{1/3}\mathcal{H}_r^{2/3}$ (where $\mathcal{H}_r = (h_1^{-2}\kappa_1 + h_2^{-2}\kappa_2)$ is the local mean curvature of the front Γ_r), and the associated propagator

$$(\partial_r + i\mathrm{Op}(p_{1,\eta}^+))\widetilde{u} = 0, \qquad \text{on } \Gamma_r. \tag{48}$$

Directly using (47)-(48) would be computationally expensive since it is a pseudodifferential nonlocal equation. In this paper, we restrict our numerical implementation to the simplest low-order model considering a zeroth-order approximation of the principal symbol corresponding to $\boldsymbol{\xi} = \mathbf{0}$. A higher order localization process based for example on a second-order Taylor expansion for small values of $||\boldsymbol{\xi}||$ would yield a second-order partial differential paraxial wave equation valid in a cone of aperture about 15 degrees in the normal direction (more details can be found in the litterature about parabolic equations models—see e.g. [27]). Considering hence the rough approximation:

$$(\partial_r - ik)\widetilde{u} = 0, \text{on } \Gamma_r, \tag{49}$$

we get the solution: $\widetilde{u}(r, \boldsymbol{s}) = e^{ikr}\widetilde{u}(0, \boldsymbol{s})$, or in other words $\widetilde{u}(\boldsymbol{x}) = \widetilde{u}(\boldsymbol{x}_0)e^{ik||\boldsymbol{x}-\boldsymbol{x}_0||}$. Since the phase $\widetilde{\phi}(\boldsymbol{x}_0)$ is known at $\boldsymbol{x}_0$ by using the OSRC approximation, the phase at point $\boldsymbol{x}$ of Ω^+ is approximated by

$$\widetilde{\phi}(\boldsymbol{x}) = \widetilde{\phi}(\boldsymbol{x}_0) + ||\boldsymbol{x} - \boldsymbol{x}_0||. \tag{50}$$

Even if we only use a very simple approximation of (43), our *a priori* complex approach is constructive and can be improved following two directions. The first one consists in using some real parabolic equations using for example the

first symbol p_1^+ and a Padé expansion to localize the resulting pseudodifferential operator (see Section 6). The second direction consists in incorporating more terms in the asymptotic expansion, e.g. computing p_0^+ (and next using some approximations, e.g. for $\boldsymbol{\xi} = \mathbf{0}$). All the corrective symbols can be obtained through some adaptations of the computations performed in [4]. However, this also implies some difficulties for the Phase Reduction approximation since special structured meshes must be used following the normal directions to solve the resulting equations. Another interesting point of our approach is that the previous construction can be adapted to variable coefficients problems like inhomogeneous Helmholtz equations. All these more advanced points are beyond the scope of the present paper and are currently being investigated.

4.2 Computing the true solution u

Since $\widetilde{\phi}$ has now been computed, we follow the same path as in the one-dimensional case. Replacing u by $\mathbb{A}e^{ik\widetilde{\phi}}$ in (18) and taking some test-functions $v = \mathbb{B}e^{ik\widetilde{\phi}}$, we obtain the alternative formulation: find $\mathbb{A} \in H^1(\Omega_b)$ such that

$$\mathcal{A}(\mathbb{A}, \mathbb{B}) = \mathcal{L}(\mathbb{B}), \tag{51}$$

for all $\mathbb{B} \in H^1(\Omega_b)$. The sesquilinear form is given by

$$\begin{aligned}\mathcal{A}(\mathbb{A}, \mathbb{B}) = (\nabla\mathbb{A}, \nabla\mathbb{B})_{0,\Omega_b} + ik\left((\mathbb{A}\nabla\widetilde{\phi}, \nabla\mathbb{B})_{0,\Omega_b} - (\nabla\mathbb{A}, \mathbb{B}\nabla\widetilde{\phi})_{0,\Omega_b}\right) \\ - k^2((1 - ||\nabla\widetilde{\phi}||^2)\mathbb{A}, \mathbb{B}))_{0,\Omega_b}(A\nabla_\Sigma\mathbb{A}, \nabla_\Sigma\mathbb{B})_{0,\Sigma} \\ + ik\left(((A\nabla_\Sigma\widetilde{\phi})\mathbb{A}, \nabla_\Sigma\mathbb{B})_{0,\Sigma} - (A\nabla_\Sigma\mathbb{A}, \mathbb{B}\nabla_\Sigma\widetilde{\phi})_{0,\Sigma}\right) \\ + k^2((A\nabla_\Sigma\widetilde{\phi}, \nabla_\Sigma\widetilde{\phi})\mathbb{A}, \mathbb{B}))_{0,\Sigma} + (\beta\mathbb{A}, \mathbb{B})_{0,\Sigma}\end{aligned} \tag{52}$$

and the linear form $\mathcal{L}$ by

$$\mathcal{L}(\mathbb{B}) = -(f, \mathbb{B})_{0,\Gamma} \tag{53}$$

with $f = ge^{-ik\widetilde{\boldsymbol{\phi}}}$ and $\widetilde{\phi}$ given. Even if the formulation seems complicated at first sight, all the quantities can be easily computed by using assembling procedures available in most basic finite element codes.

5 Numerical performance of the lowest order model

To show the improvements that can be expected from our approach using the lowest order model based on Equations (37) and (50), we begin by detailing in Section 5.1 a modal study for the sound-hard disk. Full plane wave problems are considered for the Neumann problem in Section 5.2 and for the Dirichlet problem in Section 5.3. All results were obtained using linear ($\mathbb{P}_1$) triangular

finite elements and uniform meshes. The discretization density is defined as $n_\lambda = \lambda/h$, where h measures the size of the triangles. The linear systems were solved with a sparse direct solver.

For a given approximated solution $f^{\text{calc}}(\boldsymbol{x})$, $\boldsymbol{x} \in \Omega_b$, with exact counterpart $f^{\text{exact}}(\boldsymbol{x})$, we define the relative $L^2(\Omega_b)$-error as:

$$\varepsilon_2(f) := \left\{ \int_{\Omega_b} |f^{\text{calc}}(\boldsymbol{x}) - f^{\text{exact}}(\boldsymbol{x})|^2 \, d\boldsymbol{x} \right\}^{1/2} \Big/ \left\{ \int_{\Omega_b} |f^{\text{exact}}(\boldsymbol{x})|^2 \, d\boldsymbol{x} \right\}^{1/2} \tag{54}$$

In all the following examples, f^{exact} denotes the exact solution of the *problem with the BGT2 ABC*, so that the error is not influenced by the non-perfectly transparent boundary condition.

5.1 Scattering by a sound-hard circular cylinder: mode-by-mode analysis

A first example concerns the scattering problem by a circular cylinder $\Omega^- = \mathcal{D}_0$ of radius R_0 centered at the origin. Its boundary Γ is therefore given by the circle $\Gamma = \mathcal{C}_0$. We also consider that the fictitious boundary $\Sigma = \mathcal{C}_1$ is a larger circle of radius $R_1 > R_0$, again centered at the origin. As a consequence, the bounded computational domain Ω_b is the crown delimited by the boundaries $\mathcal{C}_0$ and $\mathcal{C}_1$.

If we now consider an incident wavefield fixed by a mode of order m, that is

$$u_m^{\text{inc}}(\boldsymbol{x}) = J_m(kr)e^{im\varphi}, \qquad m \in \mathbb{Z}, \tag{55}$$

in the polar coordinates system (r, φ), then, the exact exterior modal solution to the scattering problem by the sound-hard circular cylinder $\mathcal{D}_0$ is given by

$$u_m(\boldsymbol{x}) = -\frac{J'_m(kR_0)}{H'^{(1)}_m(kR_0)} H_m^{(1)}(kr)e^{im\varphi}, \qquad r \geq R_0, \quad m \in \mathbb{Z}. \tag{56}$$

In the case where we truncate the exterior problem using the BGT2-like radiation condition (13)-(15), the analytical exact solution reads

$$u_m^{\text{exact}}(\boldsymbol{x}) = (a_m H_m^{(1)}(kr) + b_m H_m^{(2)}(kr))e^{im\varphi}, \qquad r \geq R_0, \quad m \in \mathbb{Z}, \tag{57}$$

since spurious reflection occurs at $\mathcal{C}_1$. The coefficients a_m and b_m are given by solving a 2×2 linear system of equations imposing the Neumann boundary condition at $\mathcal{C}_0$ and the ABC (13)-(15) at $\mathcal{C}_1$. This gives the following expressions

$$a_m = -\frac{A_{22} J'_m(kR_0)}{\mathrm{D}}, \qquad b_m = \frac{A_{21} J'_m(kR_0)}{\mathrm{D}}, \tag{58}$$

setting $D = A_{11}A_{22} - A_{21}A_{12}$,

$$\begin{cases} A_{11} = H_m'^{(1)}(kR_0), \qquad A_{21} = kH_m'^{(1)}(kR_1) - \mathcal{B}_m H_m^{(1)}(kR_1), \\ A_{12} = H_m'^{(2)}(kR_0), \qquad A_{22} = kH_m'^{(2)}(kR_1) - \mathcal{B}_m H_m^{(2)}(kR_1), \\ \mathcal{B}_m \;=\; -(\alpha_m \dfrac{m^2}{R_1^2} + \beta_m), \qquad \alpha_m = -\dfrac{1}{2ik}(1 + \dfrac{i}{kR_1})^{-1}, \\ \beta_m = -ik + \dfrac{1}{2R_1} + \dfrac{1}{8iR_1(1+kR_1)}. \end{cases} \tag{59}$$

Hence, being able to compute both the exact solutions to the exterior and truncated problems allow us to separate in a numerical study i) the analytical error coming from the domain truncation using the ABC (13)-(15) and ii) the error linked to the numerical approximation of the truncated problem e.g. by a finite element method. Therefore, the convergence of the numerical approximation is only visible from the exact solution u_m^{exact} given by (57)-(59) which is now considered as our reference solution for $R_0 = 1$ and $R_1 = 2$. Concerning the PR-FEM, we use the exact phase on Γ, i.e., $\phi(\theta) = cm\theta$. The reason is that the unwrapping technique cannot be applied since ϕ is not a periodic function on $[0, 2\pi]$ (unlike for the plane wave problem).

We present on Figure 4 the real parts of the wavefield u_h and $\mathbb{A}_h$ computed respectively by the FEM and the PR-FEM. We also report the absolute error compared to the exact analytical fields $u = u_m^{\text{exact}}$ and $\mathbb{A}$. The wavenumber is fixed to $k = 25$ and the density to $n_\lambda = 20$. From these computations, we observe that the field $\mathbb{A}_h$ oscillates much less than u_h. As expected, the accuracy of the FEM for computing $\mathbb{A}_h$ is higher than for u_h since less pollution arises. The mode m is propagative because $m \leq k$. This means that the rough approximation (50) is certainly not so bad. On Figure 5 we draw the evolution of the error ε_2 for $k = 50$ according to the mesh refinement for the three modes $m = 0$, $m = 25$ (both purely propagative) and $m = 50$ (which is at the transition between the region of propagative and evanescent modes). We see that the phase approximation gives an interesting improvement for the propagative part but the accuracy improvement is affected for higher harmonics where an approximate phase is much more complicated to obtain. The importance of this accuracy degradation is however moderated in practice by the fact that the solution of general scattering problems (e.g. under plane wave incidence) is a superposition of harmonics. We will see in Section 6 that higher order propagative models can capture correctly the oscillations linked to large modes even at high frequencies. We also see on Figure 5 that PR-FEM converges with the meshsize as expected for linear FEM. Second-order FEM have also been tested and lead to the expected convergence. Finally, Figure 6 shows the error behavior of the different methods for the modes $m = 0$ and $m = k$ with respect to the wavenumber. We get a higher accuracy for the PR-FEM which is again penalized for higher order harmonics m.

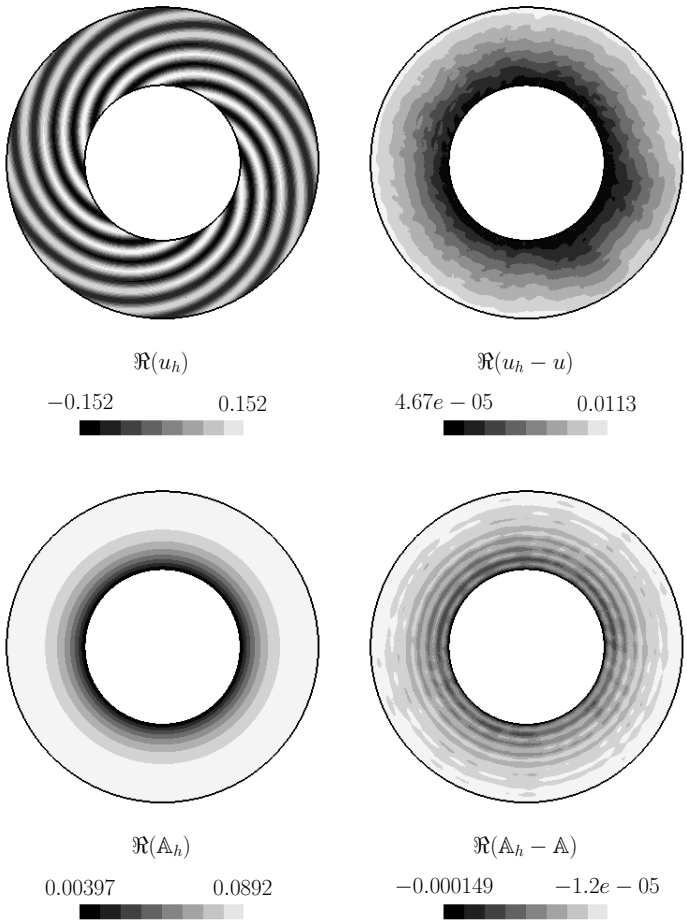

Fig. 4. Neumann problem: Real part of u_h and $\mathbb{A}_h$ and the associated errors for the mode $m = 10$. The wave number is $k = 25$ and the density is $n_\lambda = 20$.

5.2 Scattering by a sound-hard circular cylinder: plane-wave incidence

We consider an incident plane wave e^{ikx}. From now on, the PR-FEM uses the lowest-order (Sommerfeld) OSRC approximation (37). In this case, the phase $\widetilde{\phi}$ of $\widetilde{u}$ is actually the same as the phase of u^{inc} and is thus the same as the phase of the Dirichlet boundary condition. However, for completeness, the unwrapping phase technique is used to get the continuous extension of $\widetilde{\phi}$. The reason why we do not consider higher order OSRCs here is that the accuracy improvement of the starter would not be visible if high order exterior propagators are not used at the same time (this point will be analyzed in Section 6 on a simple analytical problem). Another point related to using higher order OSRCs is that we would have to refine the surface mesh just for doing the higher order OSRC (since it requires the solution of surface PDEs). It should be possible to relax this point by using two different grids—a refined $(d-1)$-dimensional grid for the OSRC computation, and a coarser d-dimensional grid for solving (51)-(53). Interpolation between the two grids could for example be performed

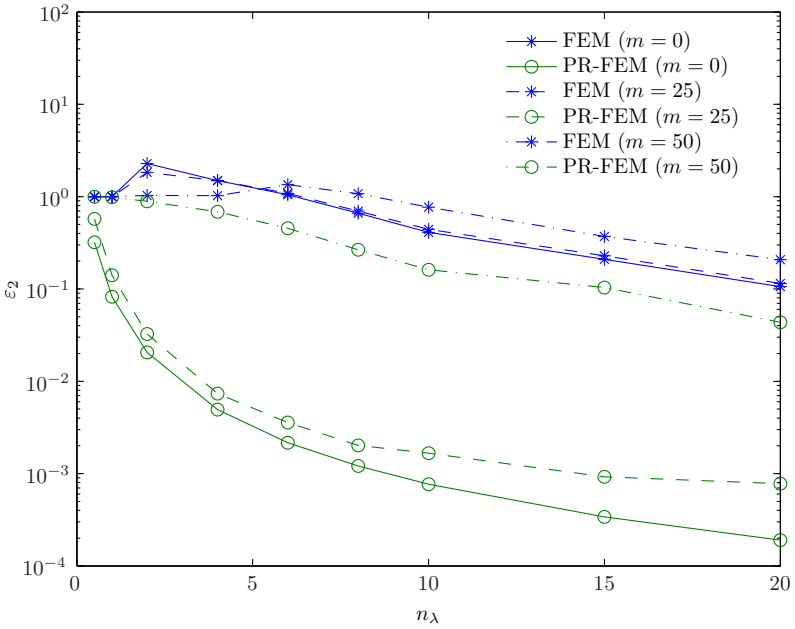

Fig. 5. Neumann problem: Evolution of the error ε_2 for several modes at $k = 50$ according to the density of discretization n_λ.

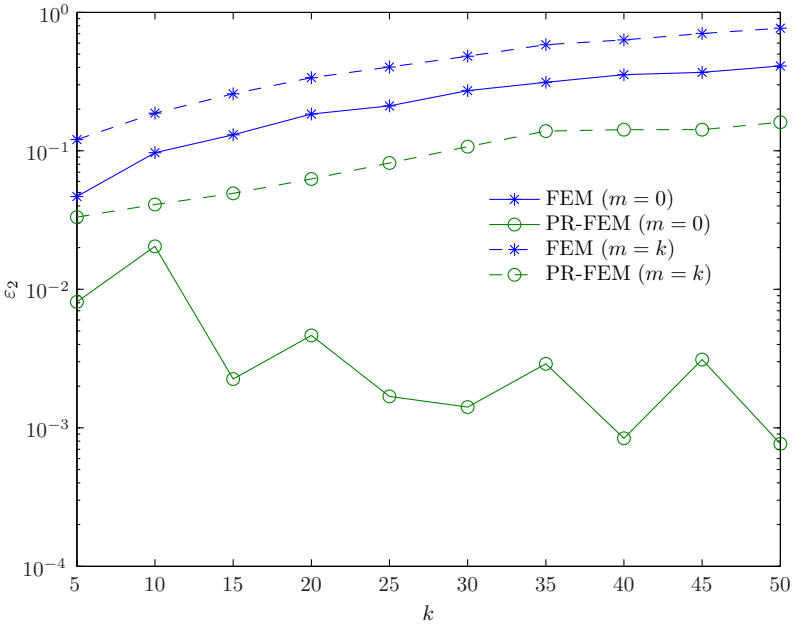

Fig. 6. Neumann problem: Evolution of the error ε_2 for the modes 0 and k with respect to the wave number k, setting $n_\lambda = 10$.

using an L^2-projection [18].

We begin by considering the same two concentric circular boundaries of Section 5.1. For a plane wave, the exact reference solution u (and so $\mathbb{A}$) is given as the linear superposition of the elementary reference solutions (using BGT2) of the previous subsection for each harmonics. We plot on Figures 7 and 8

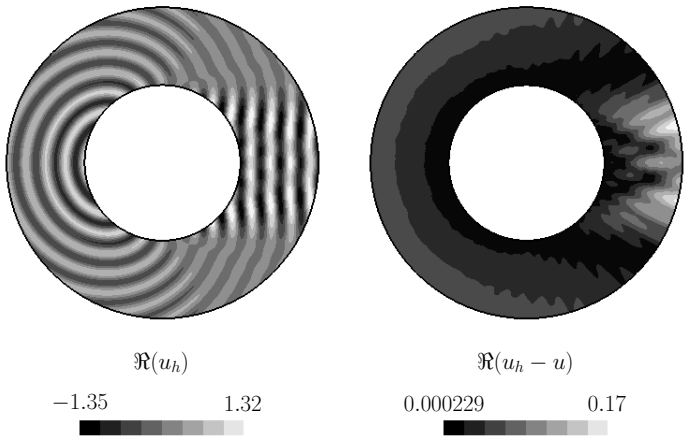

Fig. 7. Neumann problem: Real part of u_h and the associated errors. The wave number is $k = 25$ and the density is $n_\lambda = 20$.

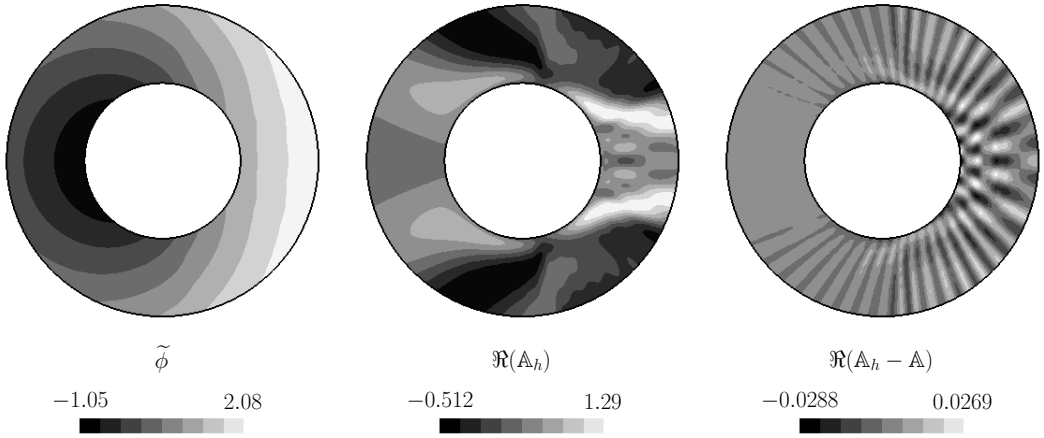

Fig. 8. Neumann problem: Approximate phase function $\widetilde{\phi}$ and real parts of $\mathbb{A}_h$ and the associated errors. The wave number is $k = 25$ and the density is $n_\lambda = 20$.

repectively the fields u_h and $\mathbb{A}_h$ and the approximate phase $\widetilde{\phi}$. We see that the finite element error is less important for the proposed formulation than for the classical formulation. Figure 9 presents the error ε_2 with respect to the wavenumber k for two different discretization densities. This again shows that the error is maintained for a fixed mesh as the wavenumber increases. The rate of convergence of the error for three different wavenumbers is reported on Figure 10. An admissible error can be obtained for low discretization densities or equivalently a higher accuracy can be expected for a fixed density. Therefore, the pollution error is reduced significantly on this example. Finally, we draw on Figure 11 the RCS for $k = 25$ and $n_\lambda = 3$. We observe a much better prediction of the far-field for these parameters when the PR-FEM is used. This is in particular clearly visible in the transition and shadow zones.

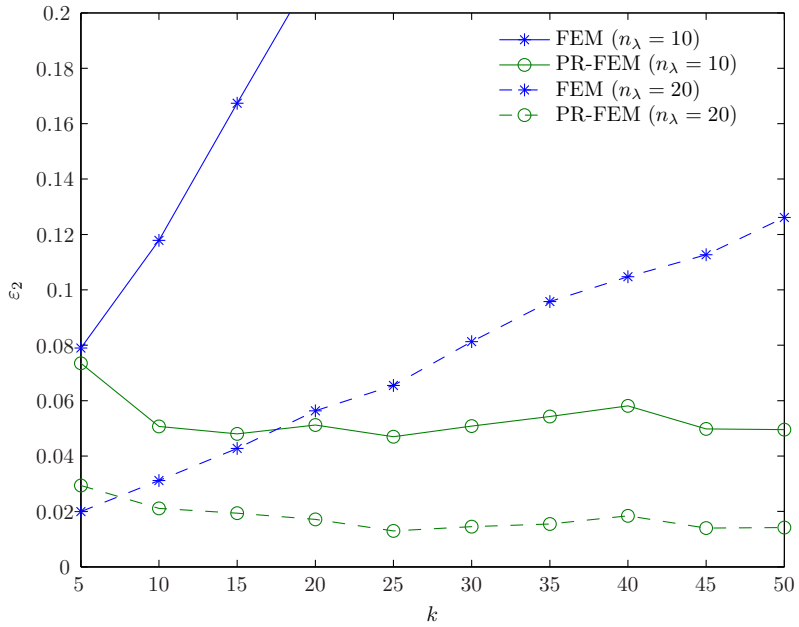

Fig. 9. Neumann problem: Evolution of the error ε_2 with respect to the wave number k for two discretizations.

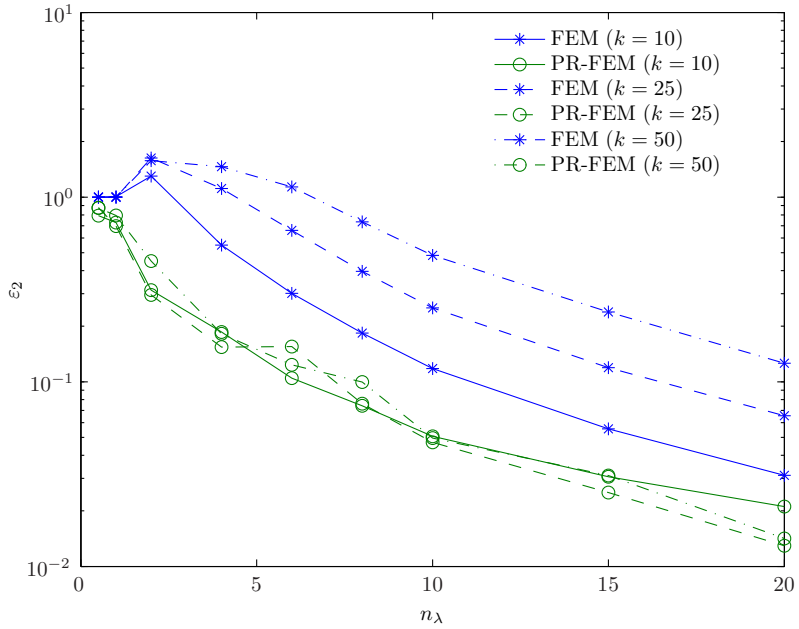

Fig. 10. Neumann problem: Evolution of the error ε_2 with respect to the density of discretization points n_λ for three wave numbers k.

5.3 Scattering by sound-soft obstacles

Let us now consider the Dirichlet problem. In this case, the starter is given immediately from the trace of the wavefield over Γ.

The first test-case is again related to the previous two concentric boundaries.

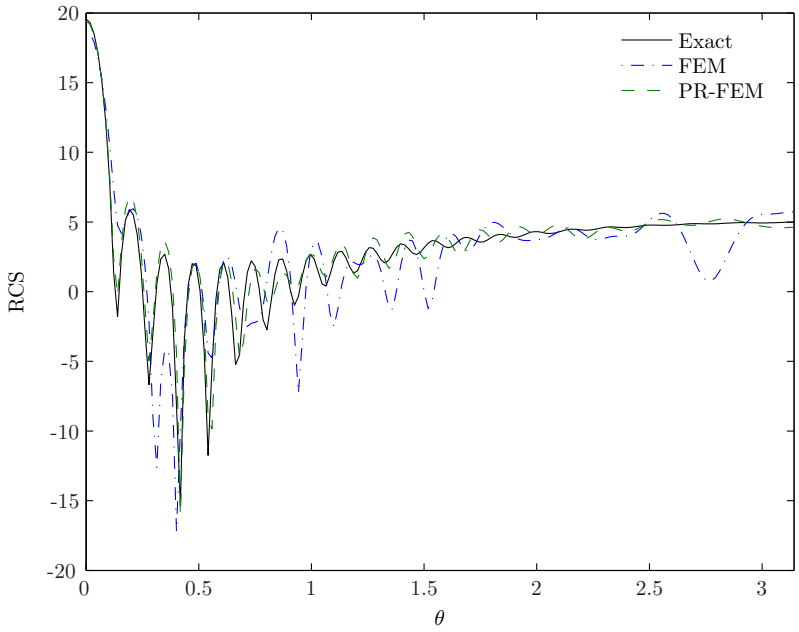

Fig. 11. Neumann problem: Bistatic Radar Cross Section for $k = 25$ and $n_\lambda = 3$.

We present on the top of Figure 13 the computed approximate phases using the low-order approximation (50) at $k = 25$. Compared to the exact solution u_h reported on Figure 12, we see that the complex amplitude $\mathbb{A}_h$ oscillates less than u_h. We report on Figure 14 the evolution of the error ε_2 with respect to k for two densities of discretization points. We can see that, compared to the classical approach, the new PR-FEM formulation even with a low-order model leads to significant accuracy improvements. Moreover, for both discretization densities n_λ, the error appears to be almost constant, which means that the pollution error has been virtually eliminated. Figure 15 presents the behavior of the error according to n_λ for three wavenumbers $k = 10$, $k = 25$ and $k = 50$. Again, the benefits of the new formulation are clearly visible: with 6 points per wavelength the relative error with the new formulation is comprised between 2.7% and 5% whereas the error with the original formulation varies between 27% and 100%.

We can expect similar gains in three dimensions. For example, the scattering problem by the unit sphere for a wavenumber $k = 10$ is considered on Figure 16, where the traces of the fields are plotted in the planes (Ox_1x_2) and (Ox_1x_3). We can see that, indeed, the field based on the slowly varying envelope $\mathbb{A}_h$ oscillates less than with the physical scattered field u_h.

To get a qualitative idea on how the PR-FEM method behaves on non-smooth geometries, we show on Figure 17 the results obtained for a thin plate under oblique plane wave incidence. The amplitude again clearly oscillates less than the original unknown, even if the reduction in the number of oscillations is less than in the case of smooth scatterers. This might be due to the low order nature of the propagator. However, as shown on Figure 18, the improvement

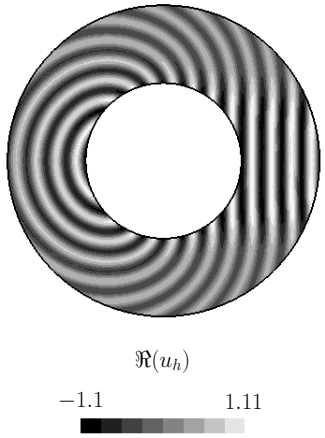

Fig. 12. Dirichlet problem: real part of the original solution u_h for $k = 25$.

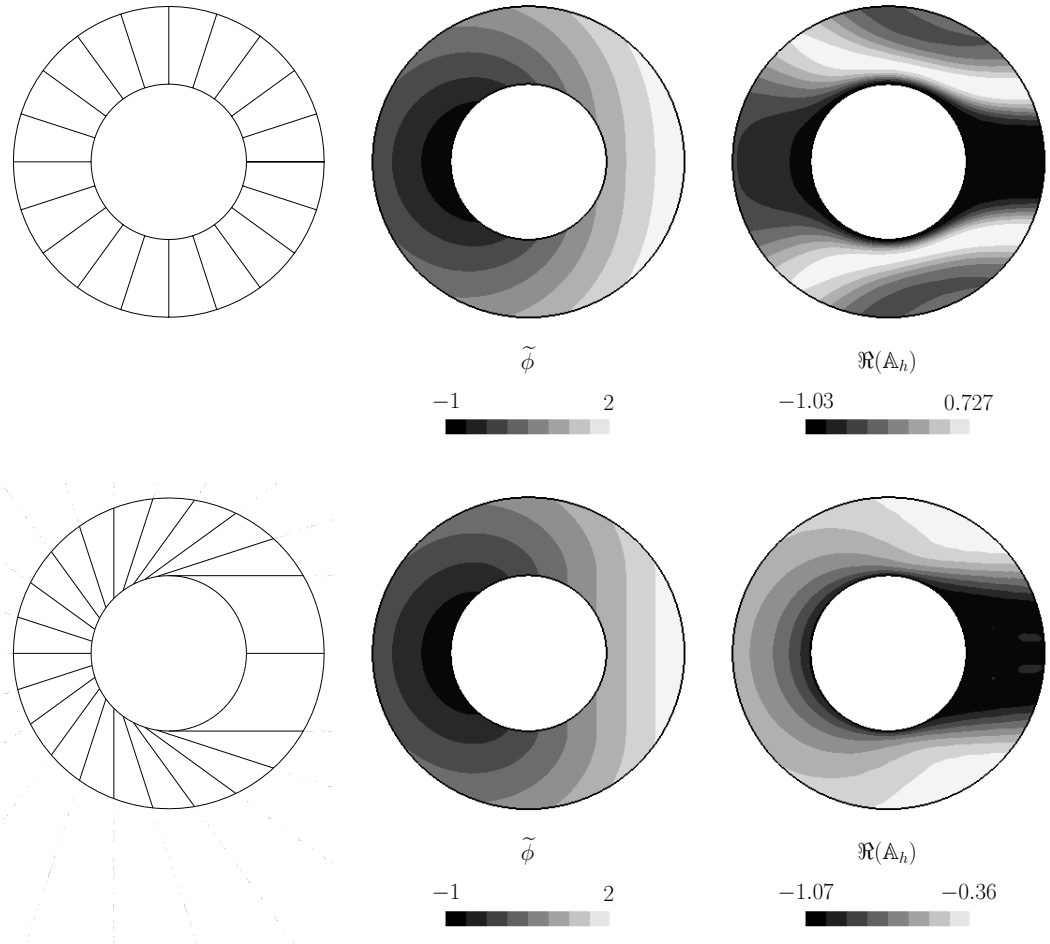

Fig. 13. Dirichlet problem: two different approximations of the phase of the complex–valued scattering solution for $k = 25$. Left: schematic depiction of the trajectories for the simple evolution equation (top) and for the eikonal equation (bottom). Middle and right: approximate phase $\widetilde{\phi}$ and real part of the resulting amplitude $\mathbb{A}_h$ for the simple evolution equation (top) and for the eikonal equation (bottom).

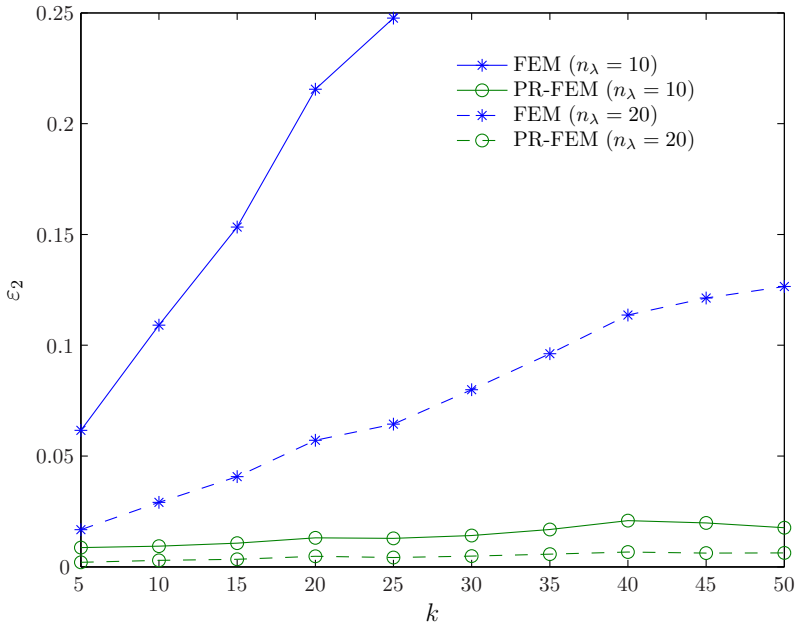

Fig. 14. Dirichlet problem: Evolution of the error ε_2 with respect to the wavenumber k for two densities of discretization points per wavelength n_λ ($n_\lambda = 10$ and $n_\lambda = 20$).

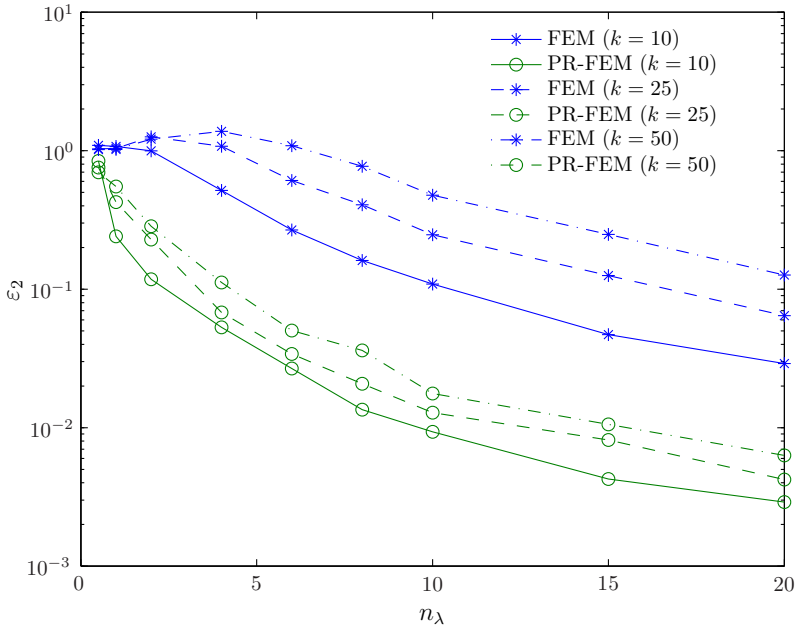

Fig. 15. Dirichlet problem: Evolution of the error ε_2 according to the density n_λ for three wavenumbers ($k = 10$, $k = 25$ and $k = 50$).

is still substantial. For $n_\lambda = 4$, the maximum error is reduced by one order of magnitude with PR-FEM. This is also true for the Neumann problem, where the low order approximation used for the starter also plays a role.

More elaborate techniques can be envisioned to approximate the phase $\phi(\boldsymbol{x})$

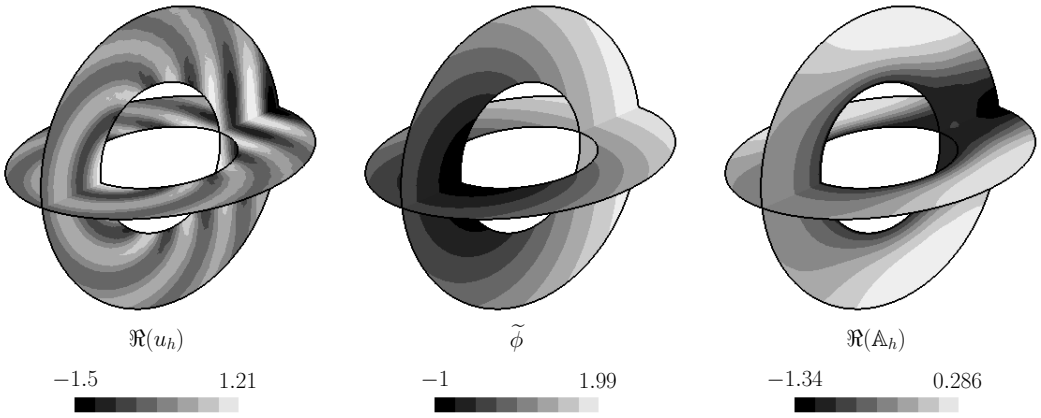

Fig. 16. Dirichlet problem: Sphere under plane wave incidence for $k = 10$. Left: real part of the original solution u_h. Middle and right: approximate phase $\widetilde{\phi}_h$ and real part of the resulting amplitude $\mathbb{A}_h$ for the simple evolution equation.

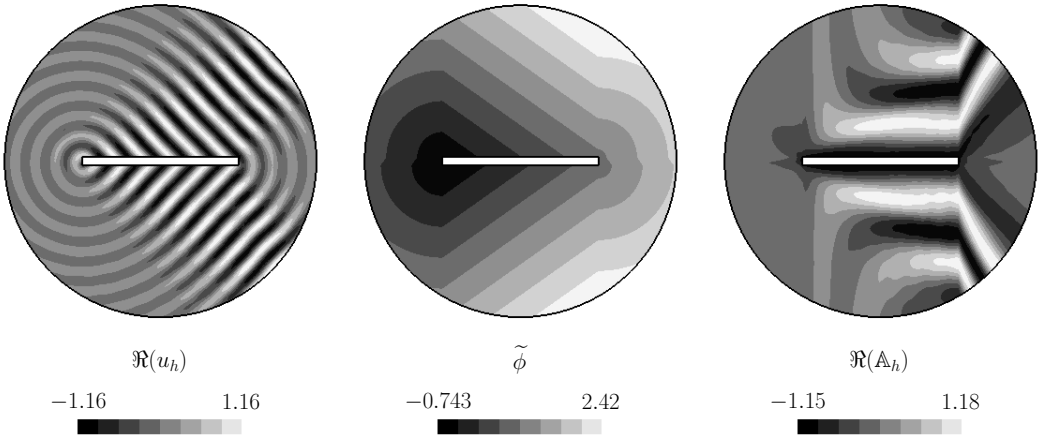

Fig. 17. Dirichlet problem: Plate under 45° plane wave incidence for $k = 25$. Left: real part of the original solution u_h. Middle and right: approximate phase $\widetilde{\phi}_h$ and real part of the resulting amplitude $\mathbb{A}_h$ for the simple evolution equation.

in the computational domain Ω. At the expense of costlier numerics, a prime candidate is to compute the phase by solving the eikonal equation

$$|\nabla\phi(\boldsymbol{x})|^2 = 1, \quad \boldsymbol{x} \in \Omega, \tag{60}$$

i.e., by using the asymptotic geometrical optics solution to the Helmholtz equation [24]. Solving Equation (60), we get a new approximate phase $\widetilde{\phi}$ and slowly varying envelope $\mathbb{A}_h$. These two fields are presented on the bottom of Figure 13. We see that the phase is close to the one expected from u_h (see Figure 12). The resulting field $\mathbb{A}_h$ therefore oscillates less than using the low-order solution. To see the impact of improving the phase computation, we report on Figure 19 the evolution of ε_2 according to the wavenumber for two coarse grids. We see that for large wave numbers, the low-order model

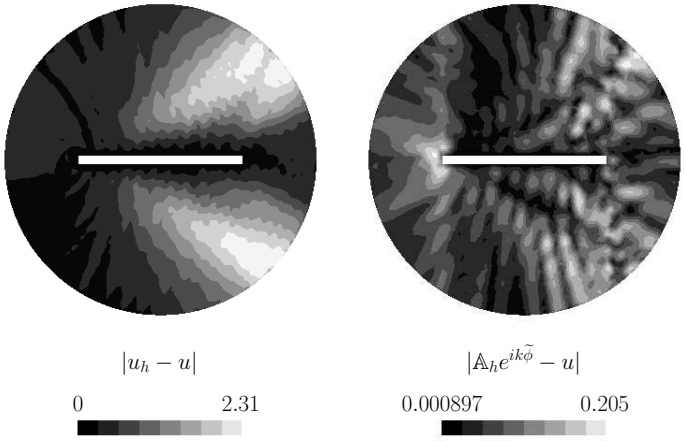

Fig. 18. Dirichlet problem: Plate under 45° plane wave incidence for $k = 25$ and $n_\lambda = 4$. Left: Absolute error between the reference solution u (computed with $n_\lambda = 20$) and the direct solution u_h. Right: Absolute error between the reference solution u and the PR-FEM solution.

attains its limitation while a very satisfying error can be expected for a better approximation of the phase using e.g. the eikonal solution. The reason of the limitation of the low-order model is that high order harmonics must be considered to compute the solution, and we showed in the mode-by-mode study developed in Section 5.1 that, indeed, high order harmonics include larger errors for the low-order model, resulting in limited accuracy of the solution for coarse meshes. As we will see in Section 6, high-order models show great potential for computing an improved phase at very high frequencies for a low computational cost. Figure 20 shows how the error evolves for a fixed mesh and increasing k. Again, a more accurate phase computation shows that an improved accuracy can be expected. The advantages of the new formulation are clearly visible: for a prescribed tolerance, the PR-FEM allows to solve the problem on much coarser grids than the original FEM, the error control depending on the phase accuracy.

6 Toward higher order models

We have seen in the previous section that an interesting accuracy improvement is obtained *via* the PR-FEM with a low-order model even for relatively high wavenumbers. At the same time, we have also shown that an increased accuracy can be expected if a better approximation of the phase is at hand, using for example the solution of the eikonal equation.

We show in this section that higher order propagative models in conjunction with an improved OSRCs can provide the phase with high accuracy, both on the surface of the scatterer and in the computational domain, even for

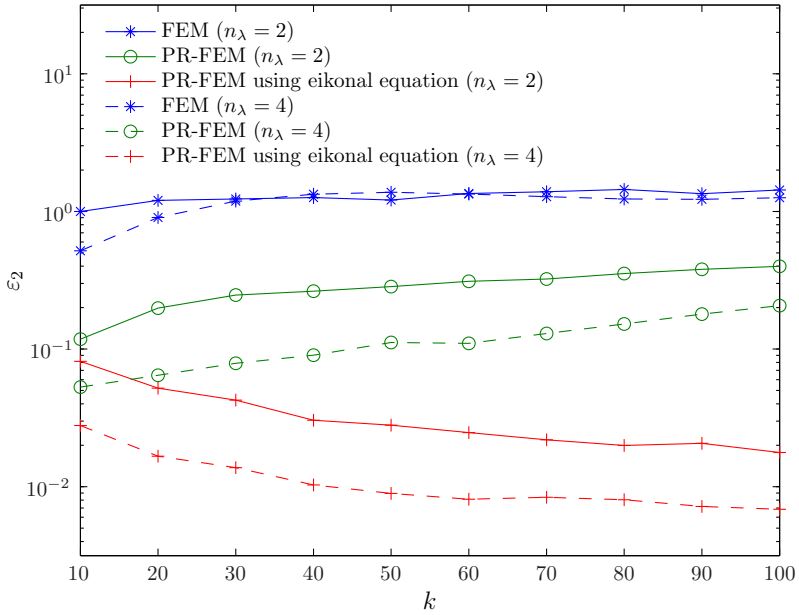

Fig. 19. Dirichlet problem: Evolution of the error ε_2 with respect to the wavenumber k for two densities of discretization points $n_\lambda = 2$ and $n_\lambda = 4$ using the classical FEM, the PR-FEM with the low-order propagator and the eikonal equation.

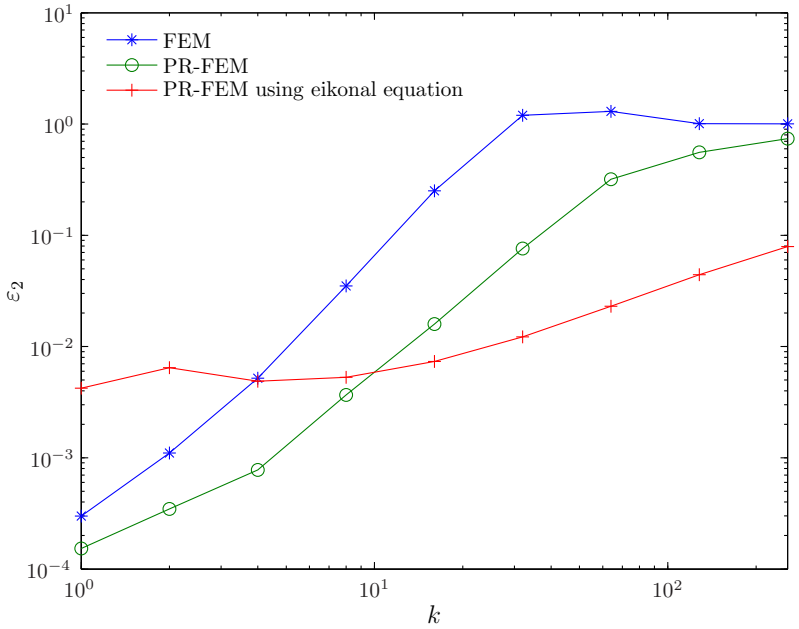

Fig. 20. Dirichlet problem: Evolution of the error ε_2 with respect to the wavenumber k ($k = 1$ to $k = 256$) using a fixed uniform mesh of 7592 triangles. The results are presented for the classical FEM, the PR-FEM with the low-order propagator and the eikonal equation.

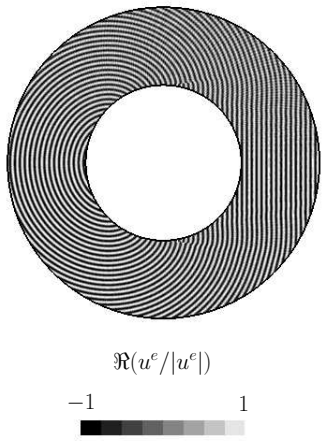

Fig. 21. Neumann problem: normalized exact solution at $k = 100$.

extremely large frequencies. An example of such high-order models is proposed in [6] using BPM techniques. Here, we consider the microlocal approximation given in Section 4 and test it in the case of the circular cylinder $\mathcal{D}_0$ with radius $R_0 = 1$ (see Section 5.1) where analytical formulae can be obtained using the mode-by-mode superposition of the solution to each problem. All the results are presented for $k = 100$ (see Figure 21); tests for a similar configuration but with $k = 2000$ for example lead to the same conclusions.

Let us introduce the following notations. For a given boundary condition (related to an OSRC operator Λ) and an exterior model (Helmholtz equation or propagator), we denote the corresponding solution by $\widetilde{u}^{BC,Model}$, where BC reflects the type of boundary condition and $Model$ the equation solved in the exterior domain:

- $BC = ik$ refers to the low-order OSRC (37) and $BC = \sqrt{}$ refers to the square-root OSRC (28);
- $Model =$ H refers to the Helmholtz equation, $Model =$ LOP refers to the low-order propagator (49) and $Model =$ HOP refers to high-order propagator (48).

Using the same notations, the slowly varying amplitudes are defined by

$$\mathbb{A}^{BC,Model} = \frac{u^{\text{exact}}}{\widetilde{u}^{BC,Model}}. \tag{61}$$

First, we test the effect of using an accurate starter based on high-order OSRCs. We report on Figure 22 the normalized real parts of the two solutions $\mathbb{A}^{ik,\mathrm{H}}$ (left) and $\mathbb{A}^{\sqrt{},\mathrm{H}}$ (right). We can observe an interesting improvement if we use the OSRC based on the square-root operator compared to the Sommerferld condition. This is particularly clear near the boundary where the modeling of surface rays is crucial. The attenuated oscillations related to us-

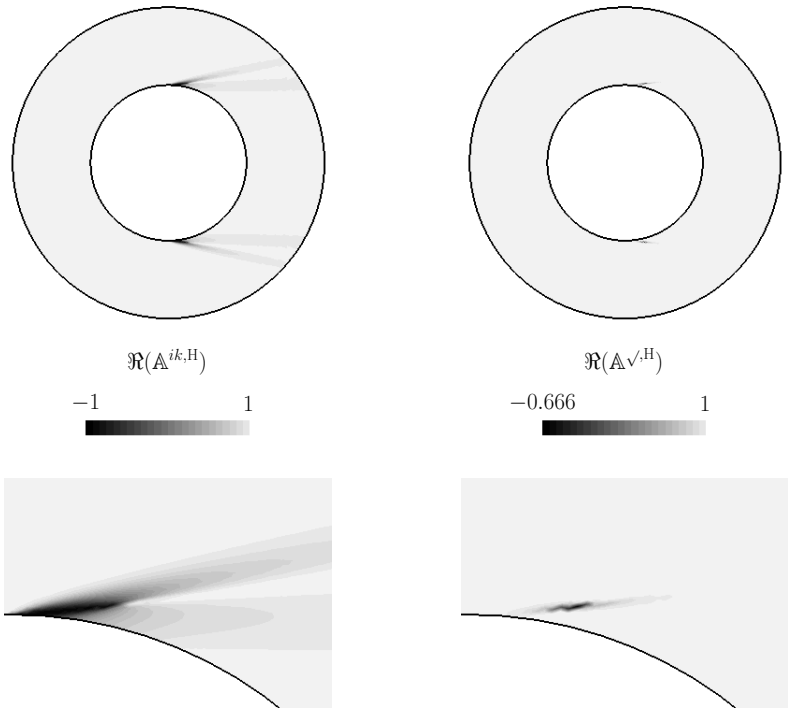

Fig. 22. Choice of the starter: Representation of $\Re(\frac{\mathbb{A}^{ik,\mathrm{H}}}{|\mathbb{A}^{ik,\mathrm{H}}|}(\boldsymbol{x}))$ (left) and $\Re(\frac{\mathbb{A}^{\surd,\mathrm{H}}}{|\mathbb{A}^{\surd,\mathrm{H}}|}(\boldsymbol{x}))$ (right) for the Neumann problem. We can observe the effect of using the low-order OSRC approximation $BC = ik$ or the high-order model $BC = \surd$. Zooming shows the boundary layer related to the incorporation of creeping waves in the OSRC model. This can affect the PR-FEM since a low-order OSRC would require a local remeshing to the surface for numerically capturing these oscillations.

ing a high-order OSRC implies that a coarser mesh should be possible close to the boundary.

Second, we test the influence of the exterior propagation equation. We have seen in Section 4.1.2 that low and high-order approximate propagators can be considered. We report on Figure 23 the real parts of $\mathbb{A}^{\surd,\mathrm{LOP}}$ and $\mathbb{A}^{\surd,\mathrm{HOP}}$. We see that using a low-order model leads to a less oscillating solution than the initial field. However, visible oscillations remain, explaining the limitations met in Section 5 when higher frequencies and/or coarser grids were considered. Using a high-order propagator solves the problem and yields a very close solution to using the Helmholtz equation (see right part of Figure 22). We can observe that even the field behavior near the boundary is satisfactory. We do not present here the numerical results obtained by using the localized Padé version of the square-root operator, which are similar to those obtained by using the square-root propagator.

Investigating PR-FEM solutions based on these two high-order generalizations shows therefore some great potential in reducing pollution problems. This is beyond the scope of the present paper and will be the subject of a second

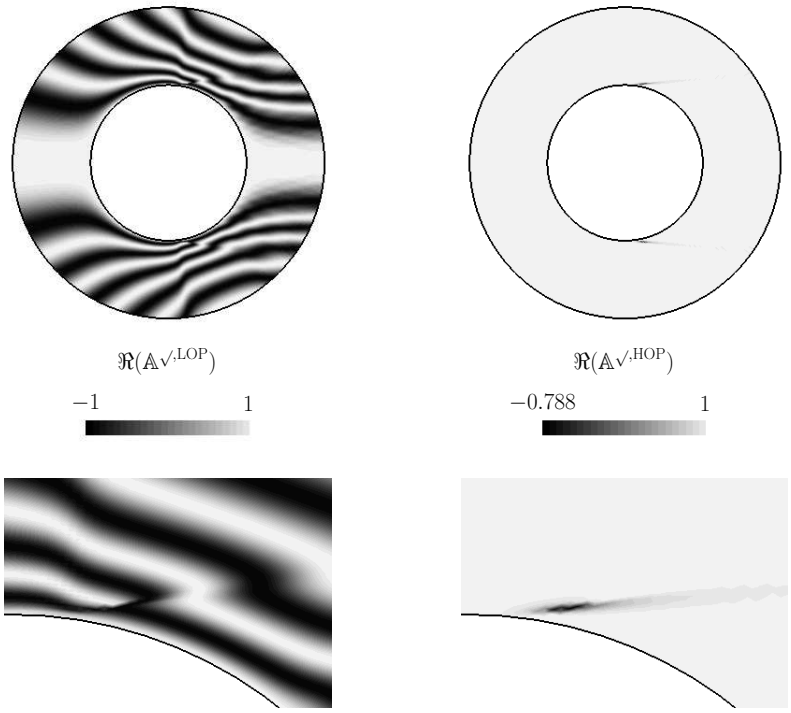

Fig. 23. Choice of the propagator: Effect of using the low-order (49) (left) or the high-order (48) propagator (right) for the Neumann problem. Zooming shows the remaining oscillations close to the boundary for the low-order model. The solution is however much less oscillating than the true solution (see Figure 21). The behavior of the near-field is close to the one expected using the Helmholtz equation (see right pictures of Figure 22). The high-order OSRC is used for building the starter.

part.

7 Conclusion

We have presented a procedure, dubbed PR-FEM, to gain significant accuracy in the finite element solution of time-harmonic scattering problems at high wavenumbers. It is based on an *a priori* approximate determination of the phase of the scattered wave using a starter/propagator technique together with a variational formulation in terms of the resulting slowly varying envelope. Numerical tests on simple two- and three-dimensional convex scatterers using the lowest-order starter/propagator model show that the technique reduces the pollution error and allows use of much coarser grids than the standard FEM. Contrary to competing approaches, the proposed method does not require any new finite element basis functions and can thus be easily implemented in existing finite element codes. Finally, accurate phase computations based on high-order starters and propagators show that improved solutions for large frequencies can be expected. This last aspect will be analyzed in Part II of

this paper.

Acknowledgement

The authors wish to thank Jacob Bedrossian for the implementation of the Eikonal equation solver. This work was supported in part by NSF under grant DMS-0609824.

References

[1] X. Antoine. Fast approximate computation of a time-harmonic scattered field using the on-surface radiation condition method. *IMA Journal of Applied Mathematics*, 66(1):83–110, 2001.

[2] X. Antoine. An algorithm coupling the OSRC and FEM for the computation of an approximate scattered acoustic field by a non-convex body. *International Journal for Numerical Methods in Engineering*, 54(7):1021–1041, 2002.

[3] X. Antoine. *Advances in the On-Surface Radiation Condition Method: Theory, Numerics and Applications*. Computational Methods for Acoustics Problems, F. Magoulès Editor, pp. 169-194. Saxe-Coburg Publications, 2008.

[4] X. Antoine, H. Barucq, and A. Bendali. Bayliss-Turkel-like radiation conditions on surfaces of arbitrary shape. *Journal of Mathematical Analysis and Applications*, 229(1):184–211, 1999.

[5] X. Antoine, M. Darbas, and Y. Y. Lu. An improved surface radiation condition for high-frequency acoustic scattering problems. *Computer Methods in Applied Mechanics and Engineering*, 195(33-36):4060–4074, 2006.

[6] X. Antoine, Y. Huang, and Y.Y. Lu. Computing high-frequency scattered fields by beam propagation methods: A prospective study. *submitted*, 2008.

[7] R. J. Astley and W. Eversman. Finite element formulations for acoustical radiation. *Journal of Sound and Vibration*, 88:47–64, 1983.

[8] R.J. Astley. Wave envelope and infinite elements for acoustical radiation. *International Journal for Numerical Methods in Fluids*, 3(5):507–526, 1983.

[9] K.J. Baumeister. Analysis of sound propagation in ducts using the wave envelope concept. Technical report, NASA TN D-7719, 1974.

[10] K.J. Baumeister. Finite-difference theory of sound propagation in ducts with variable axial dependence. In W. Strahle I.R. Schwart, H.T. Nagamatsu, editor, *Progress in Astronautics and Astronautics-Aeroacoustics: Fan noise and control; duct acoustics; rotor noise*, volume 44, pages 451–474. AIAA, New York, 1976.

[11] K.J. Baumeister. Finite difference theory for sound propagation in lined duct with uniform flow using wave envelope concept. Technical report, NASA TP 1001, 1977.

[12] K.J. Baumeister. Time-dependent wave envelope finite difference analysis of sound propagation. *AIAA Journal*, 24(1):32–38, 1986.

[13] C. M. Bender and S. A. Orszag. *Advanced Mathematical Methods for Scientists and Engineers*. McGraw-Hill, 1978.

[14] J. P. Bérenger. A perfectly matched layer for the absorption of electromagnetic waves. *Journal of Computational Physics*, 114:185–200, 1994.

[15] O. Bruno, C. Geuzaine, J. Monro, Jr., and F. Reitich. Prescribed error tolerances within fixed computational times for scattering problems of arbitrarily high frequency: the convex case. *Philosophical Transactions of the Royal Society (Series A: Mathematical, Physical and Engineering Sciences)*, 362(1816):629–645, 2004.

[16] D. Colton and R. Kress. *Integral Equation Methods in Scattering Theory*. Pure and Applied Mathematics. John Wiley and Sons, Inc., New York, 1983.

[17] C. Geuzaine, J. Bedrossian, and X. Antoine. An amplitude formulation to reduce the pollution error in the finite element solution of time-harmonic scattering problems. *IEEE Transactions on Magnetics*, 44(6):782–785, 2008.

[18] C. Geuzaine, B. Meys, P. Dular, F. Henrotte, and W. Legros. A Galerkin projection method for mixed finite elements. *IEEE Transactions on Magnetics*, 35(3):1438–1441, 1999.

[19] E. Giladi and J. B. Keller. A hybrid numerical asymptotic method for scattering problems. *Journal of Computational Physics*, 174:226–247, 2001.

[20] I. Harari, M. Slavutin, and E. Turkel. Analytical and numerical studies of a finite element PML for the Helmholtz equation. *Journal of Computational Acoustics*, 8(1):121–137, 2000.

[21] F. Ihlenburg. *Finite Element Analysis of Acoustic Scattering*. Springer, New York, 1998.

[22] F. Ihlenburg and I. Babuška. Finite element solution of the Helmholtz equation with high wave number. I. The *h*-version of the FEM. *Comput. Math. Appl.*, 30(9):9–37, 1995.

[23] F. Ihlenburg and I. Babuška. Finite element solution of the Helmholtz equation with high wave number. II. The *h-p* version of the FEM. *SIAM Journal on Numerical Analysis*, 34(1):315–358, 1997.

[24] J. B. Keller and R. M. Lewis. *Asymptotic methods for partial differential equations: the reduced wave equation and Maxwell's equations*, volume 1 of *Surveys in Applied Mathematics*, pages 1–82. Plenum Press, New York, 1995.

[25] G. A. Kriegsmann, A. Taflove, and K.R. Umashankar. A new formulation of electromagnetic wave scattering using the on-surface radiation condition method. *IEEE Transactions on Antennas and Propagation*, 35:153–161, 1987.

[26] O. Laghrouche and P. Bettess. Short wave modelling using special finite elements. *Journal of Computational Acoustics*, 8(1):189–210, 2000.

[27] M. Levy. *Parabolic Equation Methods for Electromagnetic Wave Propagation*. IEE Electromagnetic Waves Series, 45. Institution of Electrical Engineers (IEE), London, 2000.

[28] Y. Y. Lu. Some techniques for computing wave propagation in optical waveguides. *Communications in Computational Physics*, 1(6):1056–1075, 2006.

[29] F. A. Milinazzo, C. A. Zala, and G. H. Brooke. Rational square-root approximations for parabolic equation algorithms. *Journal of the Acoustical Society of America*, 101(2):760–766, 1997.

[30] Y. Saad. *Iterative Methods for Sparse Linear Systems*. PWS Pub. Co., Boston, 1996.

[31] I. M. Babuška and S.A. Sauter. Is the pollution effect of the fem avoidable for the helmholtz equation considering high wave numbers? *SIAM Review*, 42(3):451–484, 2000.

[32] M. Taylor. *Pseudodifferential Operators*. Princeton University Press, Princeton, NJ, 1981.

[33] L. L. Thompson. A review of finite element methods for time-harmonic acoustics. *Journal of the Acoustical Society of America*, 119(3):1315–1330, 2006.

[34] E. Turkel, C. Farhat, and U. Hetmaniuk. Improved accuracy for the helmholtz equation in unbounded domains. *International Journal for Numerical Methods in Engineering*, 59:1963–1988, 2004.